

Structured Illumination Microscopy Image Reconstruction Algorithm

Amit Lal, Chunyan Shan, and Peng Xi

(Invited Paper)

Abstract—Structured illumination microscopy (SIM) is a very important super-resolution microscopy technique, which provides high speed super-resolution with about two-fold spatial resolution enhancement. Several attempts aimed at improving the performance of SIM reconstruction algorithm have been reported. However, most of these highlight only one specific aspect of the SIM reconstruction—such as the determination of the illumination pattern phase shift accurately—whereas other key elements—such as determination of modulation factor, estimation of object power spectrum, Wiener filtering frequency components with inclusion of object power spectrum information, translocating and the merging of the overlapping frequency components—are usually glossed over superficially. In addition, most of the study reported lie scattered throughout the literature and a comprehensive review of the theoretical background is found lacking. The purpose of the present study is two-fold: 1) to collect the essential theoretical details of SIM algorithm at one place, thereby making them readily accessible to readers for the first time; and 2) to provide an open source SIM reconstruction code (named OpenSIM), which enables users to interactively vary the code parameters and study its effect on reconstructed SIM image.

Index Terms—Optical transfer function, structured illumination, SIM, super-resolution.

I. INTRODUCTION

OPTICAL microscopy plays critical role in life sciences study. However, the resolution of optical microscopy is limited by diffraction. The super resolution technique, owing to its ability to break this diffraction barrier has played a significant role in enabling advanced biological research, and was awarded Nobel Prize in Chemistry 2014 [1]. In the past decade, various super-resolution techniques aiming to break the diffraction barrier have been developed. These may be broadly categorized into three approaches [2]: (1) point spread function (PSF) or equivalent optical transfer function (OTF) modulation methods such as, stimulated emission depletion (STED) [3]–[6], reversible saturated excitation [7], struc-

Manuscript received October 14, 2015; revised December 29, 2015 and January 19, 2016; accepted January 21, 2016. Date of publication February 08, 2016; date of current version March 21, 2016. This work was supported by the National Instrument Development Special Program (2013YQ03065102), and the National Natural Science Foundation of China (61178076, 61475010, 31327901).

A. Lal and P. Xi are with the Department of Biomedical Engineering, College of Engineering, Peking University, Beijing 100871, China (e-mail: amitlal25999@yahoo.com; xipeng@pku.edu.cn).

C. Shan is with the School of Life Sciences, Peking University, Beijing 100871, China (e-mail: chunyanshan@pku.edu.cn).

Color versions of one or more of the figures in this paper are available online at <http://ieeexplore.ieee.org>.

Digital Object Identifier 10.1109/JSTQE.2016.2521542

tured illumination microscopy (SIM) [8]; (2) single-molecule localization methods such as, photoactivated localization microscopy (PALM) [9], [10], stochastic optical reconstruction microscopy (STORM) [11]; and (3) blinking/fluctuation statistics methods such as, super-resolution optical fluctuation imaging (SOFI) [12]–[14], spatial covariance reconstructive [15].

In live cell study, the temporal resolution is as important as the spatial resolution. However, current super-resolution techniques obtain ultra-high spatial resolution by sacrificing temporal resolution [16]. As a result, it is very difficult to apply super resolution <50 nm to *in vivo* live cell imaging. However, SIM and SOFI have demonstrated their capability in real time live cell imaging [17].

Among the super-resolution techniques, SIM is a revolutionary subset because it brings super-resolution from the perspective of frequency domain, whereas the other super-resolution techniques, such as STED, PALM/STORM, focus on modulation in spatial domain. Moreover, SIM relaxes the requirements on sample preparation dramatically; any fluorescent sample that is used in wide-field fluorescence microscopy, is compatible with SIM. Since its invention, SIM has been combined with different imaging modalities such as total-internal reflection fluorescence microscopy (TIRF) [18], surface plasmons [19], optical section with structured illumination (HiLo) [20], [21], light sheet microscopy [22], [23], quantitative fluorescence analysis [24], etc. in order to improve its resolution. It has also inspired a series of developments in super-resolution microscopy, such as saturated structured illumination microscopy [25], [26], image scanning microscopy [27], [28], SIM with speckle pattern (blind-SIM) [29], etc.

The principle of SIM OTF reconstruction was proposed by Heintzmann and Cremer in 1999 [30]. The structured illumination required can be generated by using a grating, or through digital light modulation. Due to the imperfections in the experiments, as well as the inevitable uncertainty in the measurement of experimental parameters, such as the phase and angle of illumination pattern, the SIM image reconstruction process is quite challenging. Consequently, considerable effort is devoted to development of SIM reconstruction algorithm (RA) [31]–[34]. However, most of these results lie scattered in literature, which makes it very difficult for a newcomer to see the forest with a bird's-eye view. Though some open-source SIM packages exist [35]–[37], there lacks a general open-source SIM reconstruction code, which hinders the development of the field, as one has to develop the entire SIM algorithm first rather than build on previous works.

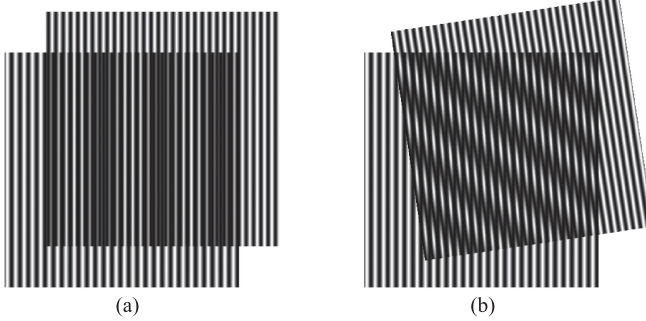


Fig. 1. Moiré pattern formation: Superposition of two *high* frequency spatial patterns results in a visually evident *low* frequency spatial pattern. Figure depicts, superposition of two sinusoidal spatial patterns when their frequency vectors, in reciprocal space, are (a) parallel and (b) non-parallel.

Recent developments in SIM RA are aimed at improving a single aspect, the accuracy of determination of the phases of sinusoidal illumination pattern [32]–[34]. However, there are other important aspects to SIM-RA too - for example, 1) determination of modulation factor, 2) translocating the separated frequency components to their correct locations in frequency space, 3) merging the overlapping frequency components effectively, etc. - which are usually glossed over superficially in SIM literature. This manuscript attempts to provide such information in detail.

Specifically, this manuscript is aimed at providing the bare-essential details, some of which are critical but often under-emphasized in literature, that are necessary to create a SIM code for reconstructing artifact-free super-resolved images. We first review the general SIM reconstruction principle (see Section III), and then present the basic SIM-RA with step by step details (see Section IV). Third, we present the simulated and experimental results (see Section VI). Finally we give the discussion and conclusion. Along with this manuscript, an open-source Matlab-based SIM-RA code is also made available, so that the readers can get an in-depth understanding, and develop further algorithms based on it. This manuscript aims at connecting the “missing links” in SIM by providing in-depth theoretical explanation along with the SIM reconstruction source code. This enables the users with biological background to understand the parameters used for optimizing the SIM reconstruction, and to modify them so that artifacts in SIM reconstructed image is reduced. The SIM-RA presented also makes a few improvements on the algorithms reported in literature.

II. SIM CONCEPT

SIM is a widefield super-resolution imaging technique in which a fluorescent labeled specimen is illuminated by a structured pattern of light intensity, typically sinusoidal, to effect Moiré pattern formation (see Fig. 1). By measuring the details of frequency content of the Moiré pattern in the observed image, and since the frequency content of illumination pattern is known beforehand, it is mathematically possible to compute the

unknown frequency content of the specimen, theoretically up to twice the frequency limit that is conventionally imposed by the OTF of the optical system. Thus, super-resolution is achieved. Mathematical details of the technique is briefly reviewed in Section III.

III. SIM FORMULATION

Let $S(\mathbf{r})$ represent fluorophore density distribution within specimen and $I_{\theta,\phi}(\mathbf{r})$ be illuminating sinusoidal intensity pattern,

$$I_{\theta,\phi}(\mathbf{r}) = I_o \left[1 - \frac{m}{2} \cos(2\pi \mathbf{p}_\theta \cdot \mathbf{r} + \phi) \right] \quad (1)$$

where $\mathbf{r} \equiv (x, y)$ is the (two dimensional) spatial position vector, I_o is peak illumination intensity, $\mathbf{p}_\theta = (p \cdot \cos \theta, p \cdot \sin \theta)$ is (sinusoidal) illumination frequency vector in reciprocal space, ϕ is phase of illumination pattern and m is modulation factor. Subscript θ indicates the orientation of sinusoidal illumination pattern. Thus, the fluorescence emission distribution from specimen is $S(\mathbf{r}) \cdot I_{\theta,\phi}(\mathbf{r})$, and the observed emission distribution through the optical system is

$$D_{\theta,\phi}(\mathbf{r}) = [S(\mathbf{r})I_{\theta,\phi}(\mathbf{r})] \otimes H(\mathbf{r}) + N(\mathbf{r}) \quad (2)$$

where $H(\mathbf{r})$ is optical system’s PSF, \otimes is convolution operator and $N(\mathbf{r})$ is additive Gaussian (white) noise.

By using convolution theorem, it may be illustrated that Fourier transform of observed image is given by (refer Supporting Information of [26])

$$\begin{aligned} \tilde{D}_{\theta,\phi}(\mathbf{k}) &= [\tilde{I}_{\theta,\phi}(\mathbf{k}) \otimes \tilde{S}(\mathbf{k})] \cdot \tilde{H}(\mathbf{k}) + \tilde{N}(\mathbf{k}) \\ &= \frac{I_o}{2} \left[\tilde{S}(\mathbf{k}) - \frac{m}{2} \tilde{S}(\mathbf{k} - \mathbf{p}_\theta) e^{-i\phi} \right. \\ &\quad \left. - \frac{m}{2} \tilde{S}(\mathbf{k} + \mathbf{p}_\theta) e^{i\phi} \right] \cdot \tilde{H}(\mathbf{k}) + \tilde{N}(\mathbf{k}) \end{aligned} \quad (3)$$

where $\tilde{H}(\mathbf{k})$ is system OTF. Equation (3) suggests that $\tilde{D}_{\theta,\phi}(\mathbf{k})$ is a linear combination of frequency content within three circular regions of specimen $\tilde{S}(\mathbf{k})$; centered at origin, $-\mathbf{p}_\theta$ and \mathbf{p}_θ in reciprocal space (see Fig. 2 c). Consequently, three different SIM images – $D_{\theta,\phi_1}(\mathbf{r})$, $D_{\theta,\phi_2}(\mathbf{r})$ and $D_{\theta,\phi_3}(\mathbf{r})$ – of the specimen is acquired corresponding to three different illumination phases; typically, $\phi_1 = 0^\circ$, $\phi_2 = 120^\circ$ and $\phi_3 = 240^\circ$. Then by Eq. (3), we have

$$\begin{bmatrix} \tilde{D}_{\theta,\phi_1}(\mathbf{k}) \\ \tilde{D}_{\theta,\phi_2}(\mathbf{k}) \\ \tilde{D}_{\theta,\phi_3}(\mathbf{k}) \end{bmatrix} = \frac{I_o}{2} \mathbf{M} \begin{bmatrix} \tilde{S}(\mathbf{k}) \tilde{H}(\mathbf{k}) \\ \tilde{S}(\mathbf{k} - \mathbf{p}_\theta) \tilde{H}(\mathbf{k}) \\ \tilde{S}(\mathbf{k} + \mathbf{p}_\theta) \tilde{H}(\mathbf{k}) \end{bmatrix} + \begin{bmatrix} \tilde{N}_{\theta,\phi_1}(\mathbf{k}) \\ \tilde{N}_{\theta,\phi_2}(\mathbf{k}) \\ \tilde{N}_{\theta,\phi_3}(\mathbf{k}) \end{bmatrix}$$

$$\text{where } \mathbf{M} = \begin{bmatrix} 1 & -\frac{m}{2} e^{-i\phi_1} & -\frac{m}{2} e^{+i\phi_1} \\ 1 & -\frac{m}{2} e^{-i\phi_2} & -\frac{m}{2} e^{+i\phi_2} \\ 1 & -\frac{m}{2} e^{-i\phi_3} & -\frac{m}{2} e^{+i\phi_3} \end{bmatrix}. \quad (4)$$

It may be noted from Eqs. (3) and (4) that the constant factor $I_o/2$ acts trivially as to scale the intensity of captured image and

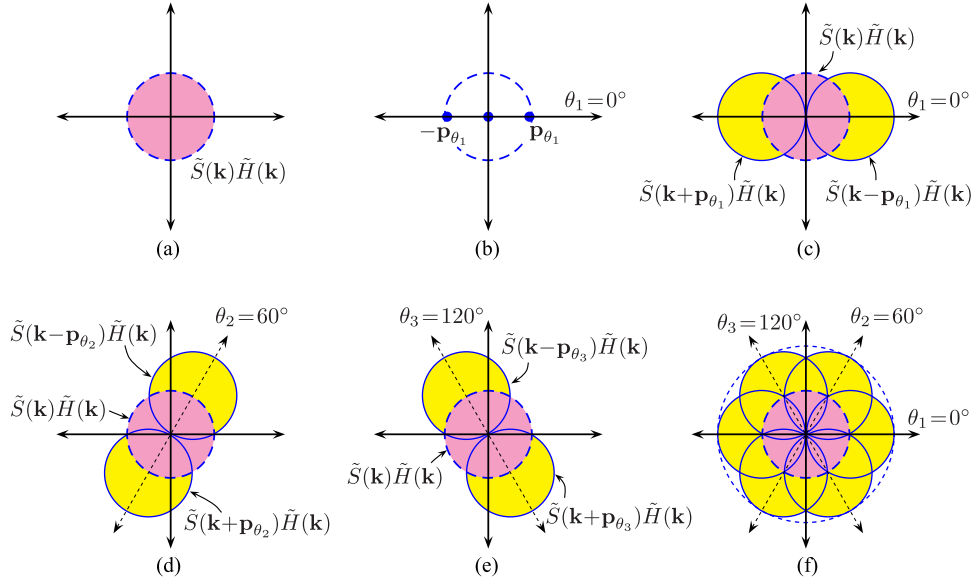


Fig. 2. SIM concept: (a) Observable frequency content of specimen in reciprocal space is limited by optical system OTF, $\tilde{H}(\mathbf{k})$. (b) Frequency content of sinusoidally varying intensity pattern (vertical stripes, $\theta_1 = 0^\circ$) relative to optical system OTF. (c,d,e) Observed frequency content of structured illuminated specimen is linear combination of frequency content within three circular regions, see Eq. (3). Note that frequency content within crescent shaped yellow regions are now observable due to Moiré effect and may be analytically computed, Eq. (5). By illuminating the specimen sequentially with sinusoidally varying illumination pattern at three different angular orientations – say 0° , 60° and 120° – specimen's frequency information till *twice* to that limited by optical system OTF may be obtained. (f) Separately obtained frequency contents are eventually merged and subsequently, used to construct super-resolved image of the specimen.

thus may be assumed to be 1. Consequently, from Eq. (4) we have

$$\text{noisy estimate of } \begin{bmatrix} \tilde{S}(\mathbf{k})\tilde{H}(\mathbf{k}) \\ \tilde{S}(\mathbf{k}-\mathbf{p}_\theta)\tilde{H}(\mathbf{k}) \\ \tilde{S}(\mathbf{k}+\mathbf{p}_\theta)\tilde{H}(\mathbf{k}) \end{bmatrix} = \mathbf{M}^{-1} \begin{bmatrix} \tilde{D}_{\theta,\phi_1}(\mathbf{k}) \\ \tilde{D}_{\theta,\phi_2}(\mathbf{k}) \\ \tilde{D}_{\theta,\phi_3}(\mathbf{k}) \end{bmatrix}. \quad (5)$$

Subsequently, the ungraded approximations of $\tilde{S}(\mathbf{k})$, $\tilde{S}(\mathbf{k}-\mathbf{p}_\theta)$ and $\tilde{S}(\mathbf{k}+\mathbf{p}_\theta)$ are obtained by Wiener filtering of their corresponding noisy estimates obtained by above equation. Finally, the centers of frequency components $\tilde{S}(\mathbf{k}-\mathbf{p}_\theta)$ and $\tilde{S}(\mathbf{k}+\mathbf{p}_\theta)$ are sub-pixelly shifted to their correct locations, $+\mathbf{p}_\theta$ and $-\mathbf{p}_\theta$ respectively, in the reciprocal space. Thus, frequency content within crescent shaped yellow regions of Fig. 2(c), which is inaccessible by direct observation, may be computed. By changing the angular orientation θ of the illuminating sinusoidal pattern (typically, three different angular orientations – say $\theta_1 = 0^\circ$, $\theta_2 = 60^\circ$ and $\theta_3 = 120^\circ$ – suffices), and by repeating the above procedure, (almost) all frequency content of specimen lying within a circular region of radius twice of that governed by the OTF of optical system may be computed (see Fig. 2(f)), enabling spatial reconstruction of specimen with twice the resolution than that which is directly obtainable using the same optical system. Thus, SIM-RA requires a set of nine different acquired images to reconstruct a super-resolved image of specimen. (Note: Though SIM reconstruction with reduced number of images [38], [39] has been demonstrated, in the present study we restrict ourselves to conventional nine-frame SIM reconstruction.)

IV. SIM RECONSTRUCTION ALGORITHM

The basic SIM-RA is presented in Algorithm 1. The essential details necessary to carry out some of the operations of the algorithm is presented in following sections.

A. Determination of Illumination Spatial Frequency \mathbf{p}_θ

In the SIM algorithm presented, illumination spatial frequency is determined *a posteriori* by iteratively optimizing the auto-correlation of $\tilde{C}_{\theta,\phi}(\mathbf{k}) = \tilde{D}_{\theta,\phi}(\mathbf{k})\tilde{H}^*(\mathbf{k})$ with its shifted variant $\tilde{C}_{\theta,\phi}(\mathbf{k} + \mathbf{p}_\theta)$:

$$\mathcal{C}_1 = \sum_{\mathbf{k}} \tilde{C}_{\theta,\phi}(\mathbf{k})\tilde{C}_{\theta,\phi}^*(\mathbf{k} + \mathbf{p}_\theta). \quad (6)$$

Value of \mathbf{p}_θ corresponding to maxima of $|\mathcal{C}_1|$ is the desired value of illumination spatial frequency.

B. Determination of Phase Shift ϕ of Illumination Pattern

Using the estimated value of illumination spatial frequency \mathbf{p}_θ above, and an (arbitrary) initial guess ϕ_o , a two dimensional sinusoidal function

$$P_{\theta,\phi_o}(\mathbf{r}) = -\cos(2\pi\mathbf{p}_\theta \cdot \mathbf{r} + \phi_o) \quad (7)$$

is constructed in the spatial domain. Using this function, an estimate of *true* phase shift is obtained by iteratively optimizing the correlation

$$\mathcal{C}_2 = \sum_{\mathbf{r}} D_{\theta,\phi}(\mathbf{r})P_{\theta,\phi_o}(\mathbf{r})$$

Algorithm 1: SIM-RA

```

1 function SIM ;
  Input : System OTF  $\tilde{H}(\mathbf{k})$  and nine raw SIM images  $D_{\theta,\phi}(\mathbf{r})$ , corresponding to  $\theta = \theta_1, \theta_2, \theta_3$  and  $\phi = \phi_1, \phi_2, \phi_3$ 
  Output: Reconstructed SIM image  $D_{SIM}(\mathbf{r})$ 
2 for  $\{D_{\theta,\phi}(\mathbf{r}) | \theta = \theta_1, \theta_2, \theta_3\}$  do
3   for  $\{D_{\theta,\phi}(\mathbf{r}) | \phi = \phi_1, \phi_2, \phi_3\}$  do
4     | Estimate illumination spatial frequency  $\mathbf{p}_\theta$  (section IV-A)
5   end
6   Take mean of the three computed values of  $\mathbf{p}_\theta$  as best estimate of illumination frequency;
7   for  $\{D_{\theta,\phi}(\mathbf{r}) | \phi = \phi_1, \phi_2, \phi_3\}$  do
8     | Estimate illumination phase shift  $\phi$  (section IV-B);
9     | /* This loop determines the three phases --  $\phi_1, \phi_2, \phi_3$  */
10    Obtain noisy estimates of  $\tilde{S}(\mathbf{k})\tilde{H}(\mathbf{k})$ ,  $\tilde{S}(\mathbf{k} - \mathbf{p}_\theta)\tilde{H}(\mathbf{k})$  and  $\tilde{S}(\mathbf{k} + \mathbf{p}_\theta)\tilde{H}(\mathbf{k})$  using Eq. (5) (do this by setting  $m = 1$  in
      matrix  $\mathbf{M}$  [Eq. (4)]; Adjustment for  $m \neq 1$  is effected later in steps 14 and 15 below) ;
11 end
12 Average the three noisy estimates of  $\tilde{S}(\mathbf{k})\tilde{H}(\mathbf{k})$  (one for each  $\theta = \theta_1, \theta_2, \theta_3$ ) and use it to estimate parameters  $\mathcal{A}$  and  $\alpha$ 
  characterizing object power spectrum (section IV-C) ;
13 for  $\theta = \theta_1, \theta_2, \theta_3$  do
14   Determine modulation factor  $m$  (section IV-D) ;
15   Use Wiener Filter to obtain noise-filtered and ungraded estimates  $\tilde{S}_u(\mathbf{k})$ ,  $\tilde{S}_u(\mathbf{k} - \mathbf{p}_\theta)$  and  $\tilde{S}_u(\mathbf{k} + \mathbf{p}_\theta)$  of noisy
       $\tilde{S}(\mathbf{k})\tilde{H}(\mathbf{k})$ ,  $\tilde{S}(\mathbf{k} - \mathbf{p}_\theta)\tilde{H}(\mathbf{k})$  and  $\tilde{S}(\mathbf{k} + \mathbf{p}_\theta)\tilde{H}(\mathbf{k})$ , respectively (section IV-E);
16   Shift  $\tilde{S}_u(\mathbf{k} - \mathbf{p}_\theta)$  and  $\tilde{S}_u(\mathbf{k} + \mathbf{p}_\theta)$  components to their respective true positions in frequency domain (section IV-F).
     Let  $\tilde{S}_s(\mathbf{k} - \mathbf{p}_\theta)$  and  $\tilde{S}_s(\mathbf{k} + \mathbf{p}_\theta)$ , respectively, denote components  $\tilde{S}_u(\mathbf{k} - \mathbf{p}_\theta)$  and  $\tilde{S}_u(\mathbf{k} + \mathbf{p}_\theta)$  shifted to their true
     positions;
17   'Phase match' the shifted components  $\tilde{S}_s(\mathbf{k} - \mathbf{p}_\theta)$  and  $\tilde{S}_s(\mathbf{k} + \mathbf{p}_\theta)$  with respect to the unshifted component  $\tilde{S}_u(\mathbf{k})$ 
     (section IV-G) ;
18 end
19 Merge all nine frequency components (three components  $\tilde{S}_u(\mathbf{k})$ ,  $\tilde{S}_s(\mathbf{k} - \mathbf{p}_\theta)$  and  $\tilde{S}_s(\mathbf{k} + \mathbf{p}_\theta)$  for each of the
  three  $\theta$ s) into one  $\tilde{D}_{SIM}(\mathbf{k})$  using generalized Wiener-Filter (section IV-H) ;
20 Compute inverse FT of  $\tilde{D}_{SIM}(\mathbf{k})$  to obtain reconstructed SIM image  $D_{SIM}(\mathbf{r})$  ;
21 return  $D_{SIM}(\mathbf{r})$  ;

```

where the summation is carried over the entire range of \mathbf{r} . Noting the similarity in sinusoidal parts of Eqs. (1) and (7), it is clear that \mathcal{C}_2 achieves its maxima when ϕ_o becomes ϕ .

C. Estimation of Object Power Spectrum

The noisy estimate of $\tilde{S}(\mathbf{k})\tilde{H}(\mathbf{k})$ that is obtained using Eq. (5) is used to determine the object's average power spectrum. As in [32], it is assumed here that average power spectrum of noisy $\tilde{S}(\mathbf{k})\tilde{H}(\mathbf{k}) = |\tilde{H}(\mathbf{k})|^2 \mathcal{A}^2 |\mathbf{k}|^{-2\alpha} + \Psi_{o,\theta}$, where \mathcal{A} and α are constants; $\Psi_{o,\theta}$ is the average noise power in $\tilde{S}(\mathbf{k})\tilde{H}(\mathbf{k})$ which may be estimated by averaging the square of frequency amplitude of (noisy) $\tilde{S}(\mathbf{k})\tilde{H}(\mathbf{k})$ over frequencies \mathbf{k} lying outside OTF support, where signal power is zero. Consequently,

$$\mathbf{M}^{-1} = \frac{1}{\Delta} \times \begin{bmatrix} e^{i(\phi_2-\phi_3)} - e^{i(\phi_3-\phi_2)} & e^{i(\phi_3-\phi_1)} - e^{i(\phi_1-\phi_3)} & e^{i(\phi_2-\phi_1)} - e^{i(\phi_1-\phi_2)} \\ \frac{2}{m} (e^{i\phi_3} - e^{i\phi_2}) & \frac{2}{m} (e^{i\phi_1} - e^{i\phi_3}) & \frac{2}{m} (e^{i\phi_2} - e^{i\phi_1}) \\ \frac{2}{m} (e^{-i\phi_2} - e^{-i\phi_3}) & \frac{2}{m} (e^{-i\phi_3} - e^{-i\phi_1}) & \frac{2}{m} (e^{-i\phi_1} - e^{-i\phi_2}) \end{bmatrix} \quad (8)$$

where $\Delta = [e^{i(\phi_2-\phi_1)} - e^{i(\phi_1-\phi_2)} - e^{i(\phi_3-\phi_1)} + e^{i(\phi_1-\phi_3)} + e^{i(\phi_3-\phi_2)} - e^{i(\phi_2-\phi_3)}]$

an iterative non-linear regression scheme is employed to obtain the optimum values of \mathcal{A} and α , characterizing object mean power spectrum. (Reasoning for $\Psi_{o,\theta}$ being independent of \mathbf{k} is discussed in Section IV-E below.)

D. Estimation of Modulation Factor m

Inverse of matrix \mathbf{M} [Eq. (4)] is given by Eq. (8) shown at the bottom of the page. This, in conjunction with Eq. (5), suggests that

$$\text{true } \tilde{S}(\mathbf{k} - \mathbf{p}_\theta)\tilde{H}(\mathbf{k}) = \frac{1}{m} \begin{bmatrix} \text{estimate of } \tilde{S}(\mathbf{k} - \mathbf{p}_\theta)\tilde{H}(\mathbf{k}) \\ \text{as computed in step 10 of} \\ \text{Algorithm 1 by setting } m = 1 \end{bmatrix}. \quad (9)$$

This relation is used to determine the modulation factor m in SIM-RA. Using the determined values of \mathcal{A} and α in Section IV-C, average power spectrum of true $\tilde{S}(\mathbf{k} - \mathbf{p}_\theta)\tilde{H}(\mathbf{k}) = |\tilde{H}(\mathbf{k})|^2 \mathcal{A}^2 |\mathbf{k} - \mathbf{p}_\theta|^{-2\alpha}$. Consequently, it follows that

$$\left. \begin{aligned} & \text{Avg. power spectrum} \\ & \text{of } \tilde{S}(\mathbf{k} - \mathbf{p}_\theta)\tilde{H}(\mathbf{k}) \\ & \text{as computed in} \\ & \text{step 10 of Algorithm 1} \end{aligned} \right\} = m^2 |\tilde{H}(\mathbf{k})|^2 \mathcal{A}^2 |\mathbf{k} - \mathbf{p}_\theta|^{-2\alpha} + \Psi_{p,\theta} \quad (10)$$

where $\Psi_{p,\theta}$ is average noise power in $\tilde{S}(\mathbf{k} - \mathbf{p}_\theta)\tilde{H}(\mathbf{k})$, as computed in step 10 of Algorithm 1, which may be determined in a manner similar to $\Psi_{o,\theta}$, as described in the previous section. Since modulation factor m is the only unknown in Eq. (10), it may be readily determined.

E. Wiener Filtering

Under the assumption that the raw SIM images are corrupted by white noise (average power spectrum of the noise is constant over all frequencies), linearity of Eqs. (4) and (5) ensures that the estimates of $\tilde{S}(\mathbf{k})\tilde{H}(\mathbf{k})$, $\tilde{S}(\mathbf{k} - \mathbf{p}_\theta)\tilde{H}(\mathbf{k})$ and $\tilde{S}(\mathbf{k} + \mathbf{p}_\theta)\tilde{H}(\mathbf{k})$ determined using Eq. (5) too are corrupted by white noise. Consequently, the ungraded estimates of $\tilde{S}(\mathbf{k})\tilde{H}(\mathbf{k})$, $\tilde{S}(\mathbf{k} - \mathbf{p}_\theta)\tilde{H}(\mathbf{k})$ and $\tilde{S}(\mathbf{k} + \mathbf{p}_\theta)\tilde{H}(\mathbf{k})$, say $\tilde{S}_u(\mathbf{k})$, $\tilde{S}_u(\mathbf{k} - \mathbf{p}_\theta)$ and $\tilde{S}_u(\mathbf{k} + \mathbf{p}_\theta)$, respectively, may be obtained by employing Wiener Filter [40], [41] as follows

$$\tilde{S}_u(\mathbf{k}) = \left[\frac{\tilde{H}^*(\mathbf{k})}{|\tilde{H}(\mathbf{k})|^2 + \frac{\Psi_{o,\theta}}{\mathcal{A}^2 |\mathbf{k}|^{-2\alpha}}} \right] \tilde{S}(\mathbf{k})\tilde{H}(\mathbf{k}) \quad (11)$$

$$\begin{aligned} \tilde{S}_u(\mathbf{k} - \mathbf{p}_\theta) &= \frac{1}{m} \left[\frac{\tilde{H}^*(\mathbf{k})}{|\tilde{H}(\mathbf{k})|^2 + \frac{\Psi_{p,\theta}}{m^2 \mathcal{A}^2 |\mathbf{k} - \mathbf{p}_\theta|^{-2\alpha}}} \right] \\ &\tilde{S}(\mathbf{k} - \mathbf{p}_\theta)\tilde{H}(\mathbf{k}) \end{aligned} \quad (12)$$

$$\begin{aligned} \tilde{S}_u(\mathbf{k} + \mathbf{p}_\theta) &= \frac{1}{m} \left[\frac{\tilde{H}^*(\mathbf{k})}{|\tilde{H}(\mathbf{k})|^2 + \frac{\Psi_{q,\theta}}{m^2 \mathcal{A}^2 |\mathbf{k} + \mathbf{p}_\theta|^{-2\alpha}}} \right] \\ &\tilde{S}(\mathbf{k} + \mathbf{p}_\theta)\tilde{H}(\mathbf{k}). \end{aligned} \quad (13)$$

Note that $\Psi_{o,\theta}$, $\Psi_{p,\theta}$ and $\Psi_{q,\theta}$ are average noise powers in $\tilde{S}(\mathbf{k})\tilde{H}(\mathbf{k})$, $\tilde{S}(\mathbf{k} - \mathbf{p}_\theta)\tilde{H}(\mathbf{k})$ and $\tilde{S}(\mathbf{k} + \mathbf{p}_\theta)\tilde{H}(\mathbf{k})$, respectively. Method of determination of $\Psi_{o,\theta}$ is described in Section IV-C; $\Psi_{p,\theta}$ and $\Psi_{q,\theta}$ may be similarly determined. The extra factor $1/m$ in Eqs. (12) and (13) accounts for the fact that in step 10 of Algorithm 1, estimates of $\tilde{S}(\mathbf{k} - \mathbf{p}_\theta)\tilde{H}(\mathbf{k})$ and $\tilde{S}(\mathbf{k} + \mathbf{p}_\theta)\tilde{H}(\mathbf{k})$ are computed by setting $m = 1$.

F. Shifting Frequency Components $\tilde{S}_u(\mathbf{k} - \mathbf{p}_\theta)$ and $\tilde{S}_u(\mathbf{k} + \mathbf{p}_\theta)$ to Their True Positions

True positions of frequency components $\tilde{S}_u(\mathbf{k} - \mathbf{p}_\theta)$ and $\tilde{S}_u(\mathbf{k} + \mathbf{p}_\theta)$ are centered respectively at frequencies \mathbf{p}_θ and $-\mathbf{p}_\theta$ in the frequency domain, see Fig. 2. By employing Fourier shift theorem [42], frequency components $\tilde{S}_u(\mathbf{k} - \mathbf{p}_\theta)$ and $\tilde{S}_u(\mathbf{k} + \mathbf{p}_\theta)$ may be shifted to their true positions, to ob-

tain their shifted variants (say) $\tilde{S}_s(\mathbf{k} - \mathbf{p}_\theta)$ and $\tilde{S}_s(\mathbf{k} + \mathbf{p}_\theta)$, respectively.

$$\mathcal{F} \left[\mathcal{F}^{-1} \left\{ \tilde{S}_u(\mathbf{k} - \mathbf{p}_\theta) \right\} \times e^{-i2\pi(\mathbf{p}_\theta \cdot \mathbf{r})} \right] = \tilde{S}_s(\mathbf{k} - \mathbf{p}_\theta) \quad (14)$$

$$\mathcal{F} \left[\mathcal{F}^{-1} \left\{ \tilde{S}_u(\mathbf{k} + \mathbf{p}_\theta) \right\} \times e^{+i2\pi(\mathbf{p}_\theta \cdot \mathbf{r})} \right] = \tilde{S}_s(\mathbf{k} + \mathbf{p}_\theta). \quad (15)$$

In the above equations, \mathcal{F} and \mathcal{F}^{-1} denotes Fourier transform and inverse Fourier transform, respectively.

G. Phase Matching

Note that from the consistency point of view,

$$\text{Arg} \left[\sum_{\mathbf{k}} \tilde{S}_u(\mathbf{k}) \tilde{S}_s^*(\mathbf{k} - \mathbf{p}_\theta) \right] = 0 \quad (16)$$

i.e., the summation of phase mismatch between *unshifted* central frequency component $\tilde{S}_u(\mathbf{k})$, obtained through Eq. (11), and *shifted* frequency component $\tilde{S}_s(\mathbf{k} - \mathbf{p}_\theta)$, obtained through Eq. (14), over the frequencies \mathbf{k} where they overlap, must be zero. However, due to inaccuracies in the determination of phases ϕ_1 , ϕ_2 , ϕ_3 , condition (16) inevitably gets violated. This calls for phase correction of shifted frequency components. The corrective phase ϕ_c is computed as

$$\phi_c = \text{Arg} \left[\sum_{\mathbf{k}} \tilde{S}_u(\mathbf{k}) \tilde{S}_s^*(\mathbf{k} - \mathbf{p}_\theta) \right] \quad (17)$$

i.e., where summation is carried over the frequencies \mathbf{k} where $\tilde{S}_u(\mathbf{k})$ and $\tilde{S}_s(\mathbf{k} - \mathbf{p}_\theta)$ overlap. Subsequently, phase correction of shifted frequency components are effected as follows

$$\begin{aligned} \text{phase} \quad & \tilde{S}_s(\mathbf{k} - \mathbf{p}_\theta) = e^{-i\phi_c} \tilde{S}_s(\mathbf{k} - \mathbf{p}_\theta) \\ \text{corrected} \quad & \tilde{S}_s(\mathbf{k} + \mathbf{p}_\theta) = e^{+i\phi_c} \tilde{S}_s(\mathbf{k} + \mathbf{p}_\theta) \end{aligned} \quad (18)$$

where $\tilde{S}_s(\mathbf{k} - \mathbf{p}_\theta)$ and $\tilde{S}_s(\mathbf{k} + \mathbf{p}_\theta)$ on right hand side of Eq. (18) are those obtained by using Eqs. (14) and (15), respectively.

H. Merging All Frequency Components Using Generalized Wiener Filter

Using “approximate” generalized Wiener filter (Eq. (44) in Appendix), triplets – $\tilde{S}_u(\mathbf{k})$, $\tilde{S}_s(\mathbf{k} - \mathbf{p}_\theta)$ and $\tilde{S}_s(\mathbf{k} + \mathbf{p}_\theta)$ – computed for each $\theta = \theta_1$, θ_2 and θ_3 may be combined to obtain Fourier transform of SIM image.

$$\begin{aligned} \tilde{D}_{\text{SIM}}(\mathbf{k}) &= \sum_{\theta=\theta_1}^{\theta_3} \left[\left(\frac{\mathcal{A}^2 |\mathbf{k}|^{-2\alpha} |\tilde{H}(\mathbf{k})|^2 / \Psi_{o,\theta}}{w + \Omega(\mathbf{k})} \right) \tilde{S}_u(\mathbf{k}) \right. \\ &+ \left(\frac{m^2 \mathcal{A}^2 |\mathbf{k} - \mathbf{p}_\theta|^{-2\alpha} |\tilde{H}(\mathbf{k} + \mathbf{p}_\theta)|^2 / \Psi_{p,\theta}}{w + \Omega(\mathbf{k})} \right) \tilde{S}_s(\mathbf{k} - \mathbf{p}_\theta) \\ &+ \left. \left(\frac{m^2 \mathcal{A}^2 |\mathbf{k} + \mathbf{p}_\theta|^{-2\alpha} |\tilde{H}(\mathbf{k} - \mathbf{p}_\theta)|^2 / \Psi_{q,\theta}}{w + \Omega(\mathbf{k})} \right) \tilde{S}_s(\mathbf{k} + \mathbf{p}_\theta) \right] \end{aligned} \quad (19)$$

where

$$\Omega(\mathbf{k}) = \sum_{\theta=\theta_1}^{\theta_3} \left[\frac{\mathcal{A}^2 |\mathbf{k}|^{-2\alpha} |\tilde{H}(\mathbf{k})|^2}{\Psi_{o,\theta}} + \frac{m^2 \mathcal{A}^2 |\mathbf{k} - \mathbf{p}_\theta|^{-2\alpha} |\tilde{H}(\mathbf{k} + \mathbf{p}_\theta)|^2}{\Psi_{p,\theta}} + \frac{m^2 \mathcal{A}^2 |\mathbf{k} + \mathbf{p}_\theta|^{-2\alpha} |\tilde{H}(\mathbf{k} - \mathbf{p}_\theta)|^2}{\Psi_{q,\theta}} \right] \quad (20)$$

and w is a constant, whose value is empirically adjusted so as to produce visibly optimum super-resolved image $D_{\text{SIM}}(\mathbf{r}) = F^{-1}[\tilde{D}_{\text{SIM}}(\mathbf{k})]$.

In the above equation, $\tilde{H}(\mathbf{k} \pm \mathbf{p}_\theta)$ is the system OTF with its center shifted to frequency vector $\pm \mathbf{p}_\theta$. However, when coordinates of $\pm \mathbf{p}_\theta$ are not integral multiple of $1/N$ ($N \times N$ pixels being digital image size), it is important *not* to use “Fourier shift theorem,” as is employed in Eqs. (14) and (15), to shift system OTF $\tilde{H}(\mathbf{k})$ to $\pm \mathbf{p}_\theta$. The shifted $\tilde{H}(\mathbf{k} \pm \mathbf{p}_\theta)$ obtained by such method is erroneous. This is a consequence of the discretization of frequencies which is inevitable while dealing with digital images and employing discrete Fourier transforms.

In the present study, the problem is resolved by observing that $\tilde{H}(\mathbf{k} \pm \mathbf{p}_\theta)$ is not explicitly required, but only its power spectrum $|\tilde{H}(\mathbf{k} \pm \mathbf{p}_\theta)|^2$ is required in Eq. (19). Consequently, an approximation $|\tilde{H}(\mathbf{k} \pm \mathbf{p}_\theta)|^2 \approx |\tilde{H}(\mathbf{k} \pm \mathbf{p}_\theta^{\text{rounded}})|^2$ is employed, where $\mathbf{p}_\theta^{\text{rounded}}$ is frequency vector obtained by rounding of coordinates of \mathbf{p}_θ to nearest integral multiple of $1/N$. Now, since coordinates of $\mathbf{p}_\theta^{\text{rounded}}$ are integral multiples of $1/N$, “Fourier shift theorem” is employed, as in Eqs. (14) and (15), to shift the system OTF $\tilde{H}(\mathbf{k})$ to $\pm \mathbf{p}_\theta^{\text{rounded}}$ and subsequently, the required power spectrum $|\tilde{H}(\mathbf{k} \pm \mathbf{p}_\theta)|^2$ is computed.

V. OPENSIM: AN OPEN SOURCE MATLAB-BASED SIM-RA CODE

The SIM-RA as described in Section IV (as well as the TIRF-SIM-RA described in Section VIII), is coded into a series of MATLAB-based script and function files. This complete set of files, collectively called as OpenSIM, is made freely available as a companion to this manuscript (see supplementary materials). This same set of files were used to obtain the results presented in Section VI.

VI. RESULTS

A. Simulation Results

To evaluate the performance of SIM-RA, a synthetic image `testpat.1k.tiff`, which is essentially an image of Lenna appended by periodic patterns of varying fineness (see Fig. 4(a)), was used. The image `testpat.1k.tiff`, referred to as “*test object*” henceforth in this manuscript, may be downloaded from USC-SIPI image database [43].

1) *Simulating raw SIM images:* The OTF $\tilde{H}(\mathbf{k})$ of the optical imaging system is assumed to be circumsymmetric with a support width as depicted Fig. 3. Consequently, Fig. 4(b) represents *noise-free* image of test object as may be acquired by the optical system. However, it assumed that images acquired by

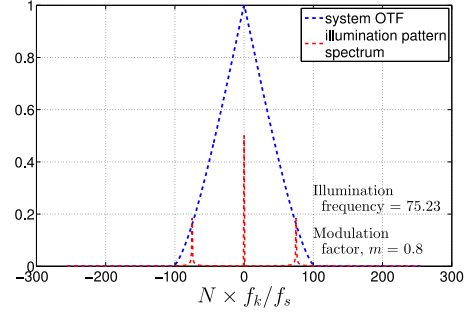


Fig. 3. OTF $\tilde{H}(\mathbf{k})$ and illumination pattern spectrum that was used for simulating raw SIM images. Note that the frequencies on the x-axis are indicated in terms of normalized frequency units: (actual frequency f_k)/(sampling frequency f_s). Since the size of the images used for generating raw SIM images is 512×512 pixels, $N = 512$.

the optical system are corrupted by an additive Gaussian noise of 10% (i.e., 20 db). Thus, Fig. 4(c) depicts a more realistic (noise corrupted) image of the test object; the effect of noise addition is prominently observed in terms of increase in grey level beyond the OTF support in Fig. 4 C.

Fig. 3 also depicts the spectrum of illumination pattern $I_{\theta,\phi}(\mathbf{r})$ [see Eq. (1)] that was used for simulating raw SIM images. As discussed in Sections IV-G, IV-H and VII-C, SIM reconstruction involves additional complications when illumination spatial frequency is not exact integral multiple $1/N$. To illustrate the effectiveness of developed SIM-RA, the illumination spatial frequency was deliberately chosen to be a fractional value, Fig. 3. The three orientations of the illumination pattern was chosen to be fixed at $\theta_1 = 0^\circ$, $\theta_2 = 60^\circ$ and $\theta_3 = 120^\circ$. However, phase shifts of the illumination pattern were assumed to be imprecise and simulated as $\phi_1 = 0^\circ + \phi_{e1}$, $\phi_2 = 120^\circ + \phi_{e2}$ and $\phi_3 = 240^\circ + \phi_{e3}$, where ϕ_{e1} , ϕ_{e2} and ϕ_{e3} are random errors with uniform probability distribution function over the range $[-15^\circ, 15^\circ]$. Precise determination of phases ϕ_1 , ϕ_2 and ϕ_3 *a posteriori* is incorporated within the SIM-RA. Fig. 4 d depicts one of the nine raw SIM images thus simulated; the frequency peaks of illumination pattern are indicated by tiny circles in Fig. 4 D.

2) *Performance of SIM algorithm:* The SIM-RA (Algorithm 1) described in Section IV was used to generate a super-resolution image (see Figs. 4(f) and (F)) of the test object using nine simulated raw SIM images (Section VI-A1). Though the enhancement in resolution of the reconstructed image in comparison to widefield image (see Fig. 4(c)) is distinctively evident both in spatial and Fourier domain, it is more appropriate to study the resolution enhancement of the reconstructed image in comparison to the deconvolved (Wiener filtered) widefield image (see Fig. 4(e)). This is because a Wiener filtering operation is intrinsically present in SIM-RA (see Section IV-E).

Visual inspection of Fig. 4(e) and (f) does reveal that the SIM reconstructed image is superior in resolution. Further, a quantitative study of resolution enhancement of the reconstructed image in comparison to the deconvolved widefield image was done by numerically determining the *effective* PSFs $\text{PSF}_{\text{deconvWF}}$ and PSF_{SIM} with which the test image (see Fig. 4(a)) when convolved, respectively, produces deconvolved widefield image (see Fig. 4(e)) and SIM reconstructed image (see Fig. 4(f)). The

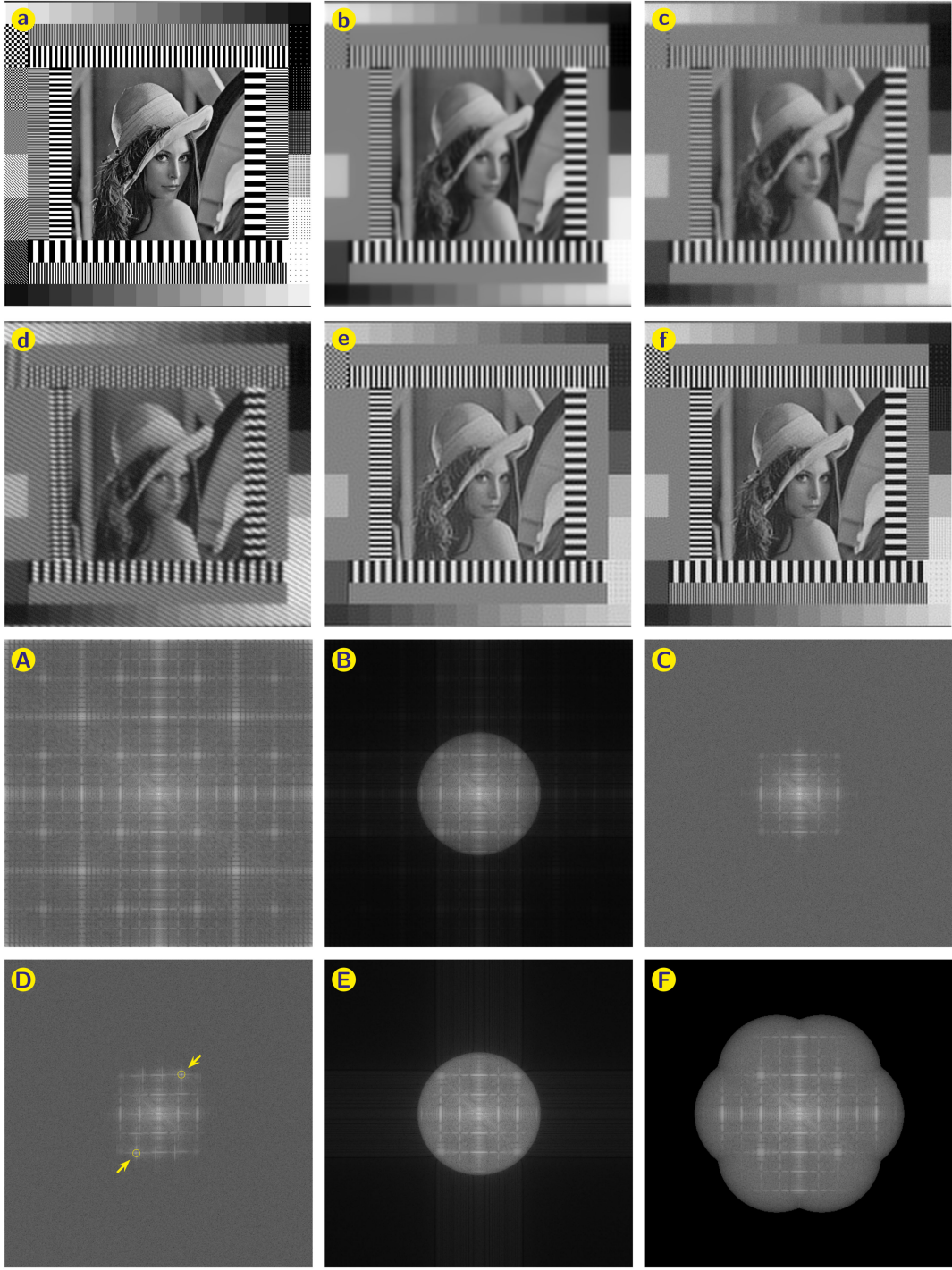


Fig. 4. (a) Test object, (b) noise free image of Test object when imaged with optical system with OTF support as depicted in Fig. 3. (c) image (b) with 10% (20 db) Gaussian noise added. (d) simulated raw SIM image with sinusoidal illumination pattern. (e) Wiener-filtered estimate of noisy image (c). Reconstructed image using SIM-RA (Algorithm 1). (A,B,...,F) Magnitude of Fourier transforms of images in (a,b,...,f).

determination of $\text{PSF}_{\text{deconvWF}}$ and PSF_{SIM} is done employing linear algebra technique (see Appendix, Section B). The numerically computed $\text{PSF}_{\text{deconvWF}}$ and PSF_{SIM} together with the imaging system PSF is depicted in Fig. 5. It may be noted that

$$\text{FWHM}(\text{PSF}_{\text{deconvWF}}) \approx 0.7 \times \text{FWHM}(\text{PSF}_{\text{system}}) \quad (21)$$

$$\text{FWHM}(\text{PSF}_{\text{SIM}}) \approx 0.5 \times \text{FWHM}(\text{PSF}_{\text{system}}). \quad (22)$$

If λ is the acquisition wavelength and NA is the numerical aperture of objective of the optical system, then $\text{FWHM}(\text{PSF}_{\text{system}}) = \lambda/(2\text{NA})$. Consequently, Eqs. (21) and (22) may be restated in a readily comprehensible form as follows

$$\text{Resolution}_{\text{(Deconv)}} \approx \frac{1}{\sqrt{2}} \frac{\lambda}{2\text{NA}} \quad (23)$$

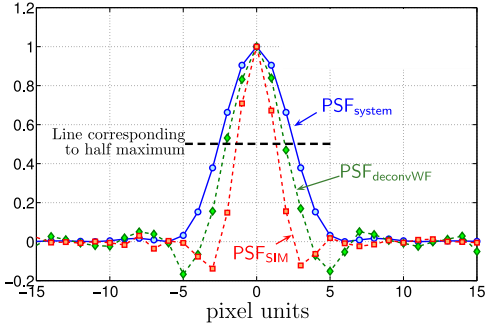


Fig. 5. Numerically computed $\text{PSF}_{\text{deconvWF}}$ and PSF_{SIM} together with imaging system PSF. Refer Section VI-A2 for further details.

$$\text{Resolution}_{(\text{SIM})} \approx \frac{1}{2} \frac{\lambda}{2\text{NA}}. \quad (24)$$

Note that $0.7 \approx 1/\sqrt{2}$; thus, Eq. (21) implies Eq. (23). Above relations between PSF widths suggest that SIM indeed improves the resolution by two-fold in spatial domain. Further, it may be noted that, the deconvolution process also improves the resolution by ≈ 1.4 fold [44].

Note that, theoretically, the maximum resolution enhancement that may be achieved through SIM-RA corresponds to $\text{FWHM}(\text{PSF}_{\text{SIM}}) = 1/2 \times \text{FWHM}(\text{PSF}_{\text{deconvWF}})$. In the present case, this limit is not achieved because (1) illumination pattern frequency is not exactly at the edge of OTF cutoff frequency, but at $\approx 75\%$ of it (see Fig. 3), and (2) the noise level in the simulated SIM raw images is not zero but 10%.

B. Experimental Results

1) *Acquisition of Raw SIM Images:* Raw SIM images of microtubules of COS7 cells, stained first with anti-alpha tubulin antibody (Active Motif) and then with goat anti-mouse secondary antibody conjuncted with Alexa Fluor 488 (Life Technologies), were obtained using an optical system with the parameters: numerical aperture NA = 1.49 (oil immersed), excitation wavelength $\lambda_{\text{ex}} = 488$ nm, emission wavelength $\lambda_{\text{em}} = 515$ nm, calibration = 60 nm/pixel. Fig. 6(a), (d) depicts one of the nine raw SIM images acquired; its fourier spectrum is represented in Fig. 6(A) (illumination spatial frequency peaks are encircled and indicated by arrows).

2) *System OTF Determination:* Several images of samples with sparsely distributed 100 nm fluorescent microspheres were obtained. Intensity distribution corresponding to more than 100 microspheres were then super-imposed and averaged to obtain an approximation for system PSF; Fourier transform of this PSF provided an estimate of system OTF.

3) *Preprocessing of Raw SIM Images:* The raw SIM images acquired experimentally were found to be corrupt with severe background fluorescence blur. Thus, raw SIM images were pre-processed in the following manner to make them suitable for SIM-RA:

- a) *Intensity normalization:* Raw SIM images were re-scaled so that all nine images have identical global mean and standard deviation.

b) *Background fluorescence removal:* The background of raw SIM fluorescent images were removed by employing in-built morphological operation function `imopen` of Matlab [45].

4) *Reconstruction of High Resolution Image Using SIM-RA:* Direct application of SIM-RA on the processed SIM images typically produces reconstructed image with hexagonal pattern artifacts. This is due to presence of residual frequency peaks in vicinity of illumination spatial frequency in $\tilde{S}_s(\mathbf{k} - \mathbf{p}_\theta)$ and $\tilde{S}_s(\mathbf{k} + \mathbf{p}_\theta)$ for each of the three θ 's resulting from inaccurate background fluorescence removal from raw SIM images; background removal techniques are heuristic in general.

In order to suppress the effect of these residual peaks resulting from the inaccuracies in background fluorescence removal, the noisy estimates of $\tilde{S}(\mathbf{k} - \mathbf{p}_\theta)\tilde{H}(\mathbf{k})$ and $\tilde{S}(\mathbf{k} + \mathbf{p}_\theta)\tilde{H}(\mathbf{k})$ obtained at step 10 of Algorithm 1 are multiplied by a heuristically designed notch filter

$$F(\mathbf{k}) = 1 - \exp(-a_o|\mathbf{k}|^\beta) \quad (25)$$

where the parameters a_o and β are real constants, values of which are set by trial and error; in the present case a_o and β were set to 0.05 and 1.2, respectively. Rest of the steps of Algorithm 1 are implemented without change. The reconstructed image obtained by application of SIM-RA is depicted in Fig. 6(d),(f). Note that the effect of notch filter $F(\mathbf{k})$ is barely visible in Fourier spectrum of reconstructed SIM image, Fig. 6(C).

For comparison, an image equivalent to the deconvolved wide-field image, obtained by Wiener filtering the averaged central frequency component $\tilde{S}(\mathbf{k})\tilde{H}(\mathbf{k})$ determined in step 12 of Algorithm 1 is shown in Fig. 6(c),(e). The enhancement in resolution in the SIM-RA reconstructed image may be readily observed.

VII. DISCUSSION

A. Determination of Illumination Spatial Frequency

In published literature, illumination spatial frequency is tacitly assumed to be known *a priori* [32]–[34]. The method used in the present study utilizes computation of auto-correlation of a single fourier image. This technique has its genesis in phase shift determination technique proposed by Wicker [34].

Note that determination of the illumination spatial frequency \mathbf{p}_θ may directly be effected by iteratively optimizing the auto-correlation too.

$$\mathcal{C}_1 = \sum_{\mathbf{k}} \tilde{D}_{\theta,\phi}(\mathbf{k}) \tilde{D}_{\theta,\phi}^*(\mathbf{k} + \mathbf{p}_\theta) \quad (26)$$

However, multiplying $\tilde{D}_{\theta,\phi}(\mathbf{k})$ with $\tilde{H}^*(\mathbf{k})$ first, and then iteratively optimizing the auto-correlation as in Eq. (6) is superior due to the following two reasons: 1) it attenuates the effect of image white noise on the calculated value of $|\mathcal{C}_1|$, and 2) in case if system PSF is asymmetric, it neutralises any disturbing effect caused by it [34]. It is remarked that reason (2) renders no advantage in determination \mathbf{p}_θ but reason (1) does. This justifies the usage of Eq. (6) for computing auto-correlation, instead of Eq. (26), in Section IV-A.

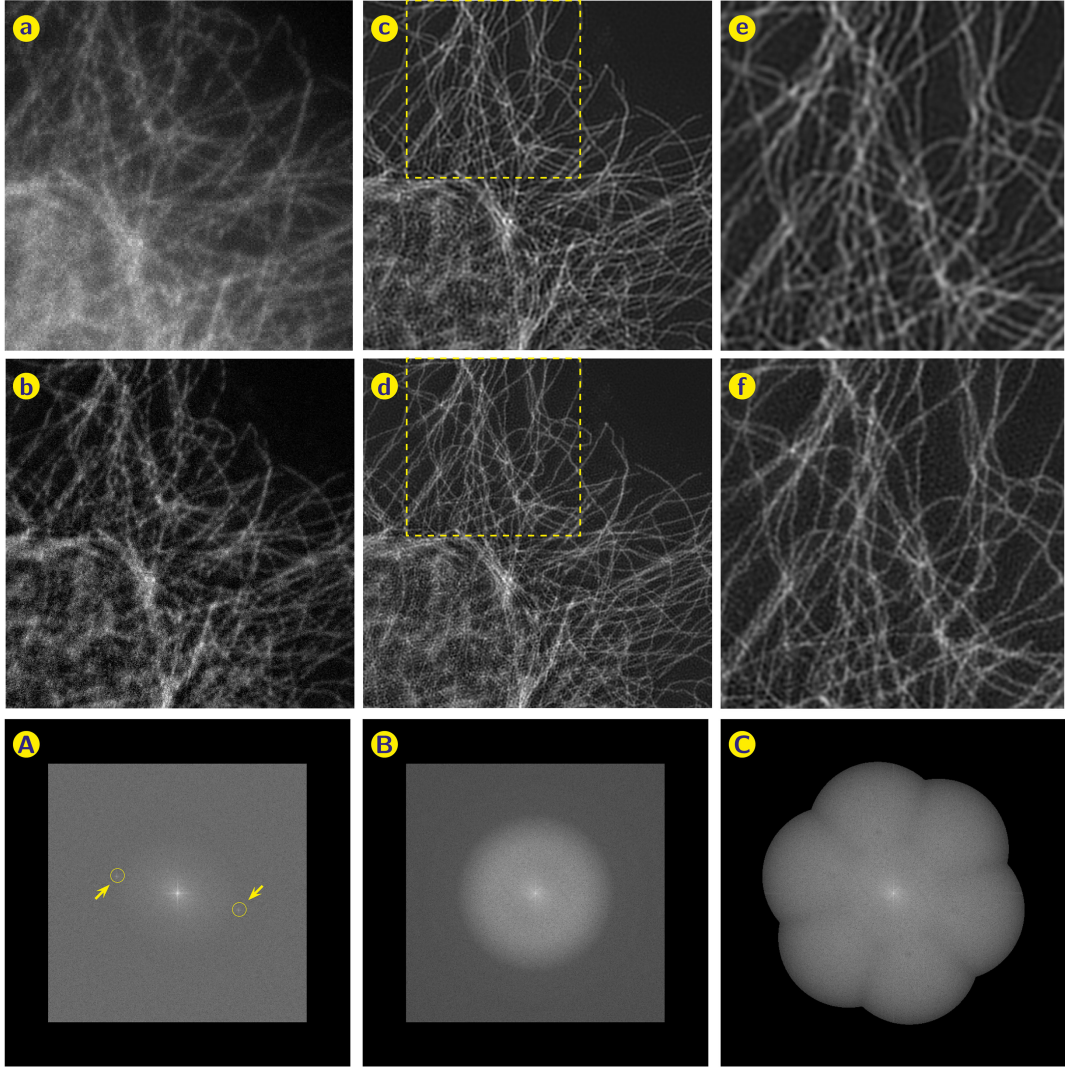


Fig. 6. (a) Experimentally acquired raw SIM image with structured illumination; its Fourier spectrum depicting the illumination spatial frequency peaks (encircled and marked by arrows) is shown in (A). (b) Raw SIM image after background subtraction; its Fourier spectrum looks apparently similar to that shown in (A) and hence is not shown. (c) Image equivalent to Wiener filtered wide-field image (refer Section VI-B4). (d) Reconstructed image $D_{\text{SIM}}(\mathbf{r})$. Images (e) and (f) are magnified views of top region, indicated by dashed frame, of images (c) and (d) respectively. Fourier spectrum of images a,c,d are indicated in A,B,C, respectively. [Specimen: Immunofluorescent staining of microtubules of COS7 cell.]

B. Determination of Illumination Phase Shift

Three different methods of illumination phase shift determination exists: 1) phase-of-peak at illumination spatial frequency of patterned image computed in Fourier domain [32], 2) iterative method based on minimizing the cross-correlation between the separated frequency components $\tilde{S}(\mathbf{k} - \mathbf{p}_\theta)\tilde{H}(\mathbf{k})$ and $\tilde{S}(\mathbf{k} + \mathbf{p}_\theta)\tilde{H}(\mathbf{k})$ (step 10 of Algorithm 1) [33], and 3) phase determination based on autocorrelation of Fourier image [34].

The potential limitations of method (1) is discussed in [32], [33]. Method (3) is illustrated to be both efficient and accurate [34]. The method essentially calls for computation of autocorrelation of $\tilde{C}_{\theta,\phi}(\mathbf{k}) = \tilde{D}_{\theta,\phi}(\mathbf{k})\tilde{H}^*(\mathbf{k})$ with its shifted variant $\tilde{C}_{\theta,\phi}(\mathbf{k} + \mathbf{p}_\theta)$:

$$C_3 = \sum_{\mathbf{k}} \tilde{C}_{\theta,\phi}(\mathbf{k})\tilde{C}_{\theta,\phi}^*(\mathbf{k} + \mathbf{p}_\theta) \quad (27)$$

following which, an estimate of illumination phase is obtained as $\phi = -\text{Arg}(\mathcal{C}_3)$. However, raw SIM images acquired experimentally were found to be corrupted with background fluorescence blur (Section VI-B3). Even though attempt is made to subtract it from the raw SIM images, its elimination is usually never perfect. Their presence introduces large errors in the frequency content of raw SIM images in a small neighborhood around zero frequency. This affects the accuracy of phase determination by both methods (2) and (3). Method (1) which, unlike methods (2) and (3), uses only *local* frequency information – peak frequency at \mathbf{p}_θ (or at $\mathbf{p}_\theta^{\text{rounded}}$ (see Section IV-H) when the coordinates of \mathbf{p}_θ are not integral multiple of $1/N$), which is far removed from the region where out-of-focus blur has erroneous effect—potentially may produce a more accurate estimate of phase ϕ (but for the effect of additive Gaussian noise).

It is for these reasons that none of the three methods were employed in the present study. Instead phase ϕ determination

was effected in spatial domain as is described in Section IV-B. The resulting estimates of phase ϕ were accurate enough to produce an artifact-free image reconstruction even for experimental case, Fig. 6.

Note that for both simulated and experimental data, illumination spatial frequency lie within the system OTF support. The method described in Section IV-B does not study when illumination spatial frequency lies beyond the system OTF support, as in TIRF-SIM. In such a case, iterative Method (2) described above is used. Section VIII describes a variant of Algorithm 1 that may be used to carry out reconstruction of SIM image when raw SIM images are obtained using a TIRF-SIM setup.

C. Approximation for Generalized Wiener Filter

Direct usage of generalized Wiener filter, as presented in Eq. (42), for merging the separated components cannot be done in practice. This is because, if $\tilde{G}_i(\mathbf{k}) = \tilde{S}_i(\mathbf{k})\tilde{H}_i(\mathbf{k})$, and $\tilde{G}_i(\mathbf{k} + \mathbf{p}_\theta)$, $\tilde{S}_i(\mathbf{k} + \mathbf{p}_\theta)$ and $\tilde{H}_i(\mathbf{k} + \mathbf{p}_\theta)$ are shifted forms of $\tilde{G}_i(\mathbf{k})$, $\tilde{S}_i(\mathbf{k})$ and $\tilde{H}_i(\mathbf{k})$, respectively, to frequency center \mathbf{p}_θ , obtained using Fourier shift theorem, then $\tilde{G}_i(\mathbf{k} + \mathbf{p}_\theta) \neq \tilde{S}_i(\mathbf{k} + \mathbf{p}_\theta)\tilde{H}_i(\mathbf{k} + \mathbf{p}_\theta)$ when coordinates of \mathbf{p}_θ are not integral multiple of $1/N$. Therefore, instances where equation of generalized Wiener filter, similar to Eq. (42), is presented in SIM literature, for example [32], [33], are only meant to convey the general “conceptual idea” and *not* the direct methodology for merging the separated frequency components.

Practical implementation of generalized Wiener filter necessarily requires approximations to be made and has an element of art to it; Gustafsson *et al.* [46] have rightly used the adjective “*somewhat non-intuitive*” to characterize the methodology of implementing generalized Wiener filter. The methodology presented in this manuscript, closely adheres to the approach suggested by Gustafsson *et al.* [46]. Moreover, the present study makes the approach more explicit by presenting it in the form of a concrete algorithm.

D. Apodization Filter

Usage of an apodization filter $\tilde{A}(\mathbf{k})$ is advocated in some SIM-RA, refer [33] for instance. In these algorithms, $\tilde{D}_{\text{SIM}}(\mathbf{k})$, as computed by Eq. (19), is multiplied by $\tilde{A}(\mathbf{k})$, and then the SIM reconstructed image is computed as $D_{\text{SIM}}(\mathbf{r}) = \mathcal{F}^{-1} [\tilde{D}_{\text{SIM}}(\mathbf{k})\tilde{A}(\mathbf{k})]$. An appropriately designed apodization filter helps avoid hard edges and ringing effect that may arise in reconstructed image $D_{\text{SIM}}(\mathbf{r})$ otherwise.

In the present study, SIM reconstruction for the simulated case (see Fig. 4) is done without apodization filter, but for the experimental case (see Fig. 6) it was done using an apodization filter. OpenSIM package accompanied with this manuscript also possesses a subroutine to apodize filter $\tilde{D}_{\text{SIM}}(\mathbf{k})$, as computed by Eq. (19), prior to reconstruction of SIM image. The apodization filter $\tilde{A}(\mathbf{k})$ incorporated in OpenSIM is identical with that described in [33].

E. Customizing SIM-RA for Experimental Data

Pre-processing of raw SIM images as described in Section VI-B3 is necessary. Intensity normalization compensates for

variations in overall intensities among the nine raw SIM images. Background fluorescence removal reduces the overall blur in the reconstructed SIM image, which tends to mask the resolution enhancement. Since background fluorescence removal is realized heuristically, it is essential to employ a notch filter of the kind illustrated in Eq. (25) to suppress residual peaks in lateral frequency components resulting from inaccuracies in background fluorescence removal. Such customization of SIM-RA is specific to the nature of experimental data and is done empirically.

VIII. TIRF-SIM ALGORITHM

In a TIRF-SIM setup, the illumination spatial frequency typically lies beyond the system OTF support. This section describes a variant of Algorithm 1 that may be used to carry out reconstruction of SIM image when the raw SIM images are obtained using a TIRF-SIM setup.

A. Formulation

Defining

$$\tilde{S}_o(\mathbf{k} - \mathbf{p}_\theta) = e^{-i\phi_1} \tilde{S}(\mathbf{k} - \mathbf{p}_\theta) \quad (28)$$

$$\tilde{S}_o(\mathbf{k} + \mathbf{p}_\theta) = e^{+i\phi_1} \tilde{S}(\mathbf{k} + \mathbf{p}_\theta) \quad (29)$$

$$\phi'_2 = \phi_2 - \phi_1 \quad (30)$$

$$\phi'_3 = \phi_3 - \phi_1. \quad (31)$$

Eq. (4) may be rewritten as

$$\begin{bmatrix} \tilde{D}_{\theta,\phi_1}(\mathbf{k}) \\ \tilde{D}_{\theta,\phi_2}(\mathbf{k}) \\ \tilde{D}_{\theta,\phi_3}(\mathbf{k}) \end{bmatrix} = \frac{I_o}{2} \mathbf{M}_o \begin{bmatrix} \tilde{S}(\mathbf{k})\tilde{H}(\mathbf{k}) \\ \tilde{S}_o(\mathbf{k} - \mathbf{p}_\theta)\tilde{H}(\mathbf{k}) \\ \tilde{S}_o(\mathbf{k} + \mathbf{p}_\theta)\tilde{H}(\mathbf{k}) \end{bmatrix} + \begin{bmatrix} \tilde{N}_{\theta,\phi_1}(\mathbf{k}) \\ \tilde{N}_{\theta,\phi_2}(\mathbf{k}) \\ \tilde{N}_{\theta,\phi_3}(\mathbf{k}) \end{bmatrix} \quad (32)$$

$$\text{where } \mathbf{M}_o = \begin{bmatrix} 1 & -\frac{m}{2} & -\frac{m}{2} \\ 1 & -\frac{m}{2}e^{-i\phi'_2} & -\frac{m}{2}e^{+i\phi'_2} \\ 1 & -\frac{m}{2}e^{-i\phi'_3} & -\frac{m}{2}e^{+i\phi'_3} \end{bmatrix}. \quad (33)$$

Setting $I_o/2 = 1$, analogous to Eq. (5), we have

$$\begin{array}{ll} \text{noisy} & \begin{bmatrix} \tilde{S}(\mathbf{k})\tilde{H}(\mathbf{k}) \\ \tilde{S}_o(\mathbf{k} - \mathbf{p}_\theta)\tilde{H}(\mathbf{k}) \\ \tilde{S}_o(\mathbf{k} + \mathbf{p}_\theta)\tilde{H}(\mathbf{k}) \end{bmatrix} \\ \text{estimate} & = \mathbf{M}_o^{-1} \begin{bmatrix} \tilde{D}_{\theta,\phi_1}(\mathbf{k}) \\ \tilde{D}_{\theta,\phi_2}(\mathbf{k}) \\ \tilde{D}_{\theta,\phi_3}(\mathbf{k}) \end{bmatrix} \\ \text{of} & \end{array} \quad (34)$$

B. Determination of Phases ϕ'_2 and ϕ'_3

Let ψ_2 and ψ_3 be *approximate* estimates of ϕ'_2 and ϕ'_3 , respectively. Then, approximation to \mathbf{M}_o would be

$$\mathbf{M}_e = \begin{bmatrix} 1 & -\frac{1}{2} & -\frac{1}{2} \\ 1 & -\frac{1}{2}e^{-i\psi_2} & -\frac{1}{2}e^{+i\psi_2} \\ 1 & -\frac{1}{2}e^{-i\psi_3} & -\frac{1}{2}e^{+i\psi_3} \end{bmatrix}$$

and $\mathbf{M}_e^{-1} =$

$$\frac{1}{\Delta_e} \begin{bmatrix} e^{i(\psi_2 - \psi_3)} - e^{i(\psi_3 - \psi_2)} & e^{i\psi_3} - e^{-i\psi_3} & e^{i\psi_2} - e^{-i\psi_2} \\ 2(e^{i\psi_3} - e^{i\psi_2}) & 2(1 - e^{i\psi_3}) & 2(e^{i\psi_2} - 1) \\ 2(e^{-i\psi_2} - e^{-i\psi_3}) & 2(e^{-i\psi_3} - 1) & 2(1 - e^{-i\psi_2}) \end{bmatrix} \quad (35)$$

where

$$\Delta_e = [e^{i\phi_2} - e^{-i\psi_2} - e^{i\psi_3} + e^{-i\psi_3} + e^{i(\psi_3 - \psi_2)} - e^{i(\psi_2 - \psi_3)}].$$

Let $\tilde{S}_a(\mathbf{k})\tilde{H}(\mathbf{k})$, $\tilde{S}_a(\mathbf{k} - \mathbf{p}_\theta)\tilde{H}(\mathbf{k})$ and $\tilde{S}_a(\mathbf{k} + \mathbf{p}_\theta)\tilde{H}(\mathbf{k})$ be noisy estimates of $\tilde{S}(\mathbf{k})\tilde{H}(\mathbf{k})$, $\tilde{S}_o(\mathbf{k} - \mathbf{p}_\theta)\tilde{H}(\mathbf{k})$ and $\tilde{S}_o(\mathbf{k} + \mathbf{p}_\theta)\tilde{H}(\mathbf{k})$, respectively, when ψ_2 and ψ_3 are used as approximate estimates ϕ'_2 and ϕ'_3 . Then, from Eq. (34) we have

$$\begin{aligned} \begin{bmatrix} \tilde{S}_a(\mathbf{k})\tilde{H}(\mathbf{k}) \\ \tilde{S}_a(\mathbf{k} - \mathbf{p}_\theta)\tilde{H}(\mathbf{k}) \\ \tilde{S}_a(\mathbf{k} + \mathbf{p}_\theta)\tilde{H}(\mathbf{k}) \end{bmatrix} &= \mathbf{M}_e^{-1} \begin{bmatrix} \tilde{D}_{\theta, \phi_1}(\mathbf{k}) \\ \tilde{D}_{\theta, \phi_2}(\mathbf{k}) \\ \tilde{D}_{\theta, \phi_3}(\mathbf{k}) \end{bmatrix} \\ &= \mathbf{M}_e^{-1} \mathbf{M}_o \begin{bmatrix} \tilde{S}(\mathbf{k})\tilde{H}(\mathbf{k}) \\ \tilde{S}_o(\mathbf{k} - \mathbf{p}_\theta)\tilde{H}(\mathbf{k}) \\ \tilde{S}_o(\mathbf{k} + \mathbf{p}_\theta)\tilde{H}(\mathbf{k}) \end{bmatrix} \end{aligned} \quad (36)$$

where Eq. (32) is used in the last equality; noise term is ignored for compactness. The above equation may be solved to obtain

$$\begin{bmatrix} \tilde{S}_a(\mathbf{k} - \mathbf{p}_\theta)\tilde{H}(\mathbf{k}) \\ \tilde{S}_a(\mathbf{k} + \mathbf{p}_\theta)\tilde{H}(\mathbf{k}) \end{bmatrix} = \frac{m}{\Delta_e} \begin{bmatrix} a_{22} & a_{23} \\ a_{32} & a_{33} \end{bmatrix} \begin{bmatrix} \tilde{S}_o(\mathbf{k} - \mathbf{p}_\theta)\tilde{H}(\mathbf{k}) \\ \tilde{S}_o(\mathbf{k} + \mathbf{p}_\theta)\tilde{H}(\mathbf{k}) \end{bmatrix} \quad (37)$$

where

$$\begin{aligned} a_{22} &= e^{i\psi_2} - e^{-i\phi'_2} - e^{i\psi_3} + e^{-i\phi'_3} + e^{i(\psi_3 - \phi'_2)} - e^{i(\psi_2 - \phi'_3)} \\ a_{23} &= e^{i\psi_2} - e^{i\phi'_2} - e^{i\psi_3} + e^{i\phi'_3} + e^{i(\psi_3 + \phi'_2)} - e^{i(\psi_2 + \phi'_3)} \\ a_{32} &= e^{-i\phi'_2} - e^{-i\psi_2} - e^{-i\phi'_3} + e^{-i\psi_3} + e^{-i(\phi'_3 + \psi_2)} \\ &\quad - e^{-i(\phi'_2 + \psi_3)} \\ a_{33} &= e^{i\phi'_2} - e^{-i\psi_2} - e^{i\phi'_3} + e^{-i\psi_3} + e^{i(\phi'_3 - \psi_2)} - e^{i(\phi'_2 - \psi_3)}. \end{aligned}$$

Note that $a_{23} = 0$ and $a_{32} = 0$ only when $\psi_2 = \phi'_2$ and $\psi_3 = \phi'_3$. For this condition, referring to Eq. (37), $\tilde{S}_a(\mathbf{k} - \mathbf{p}_\theta)\tilde{H}(\mathbf{k}) = m\tilde{S}_o(\mathbf{k} - \mathbf{p}_\theta)\tilde{H}(\mathbf{k})$ and has no contribution from $\tilde{S}_o(\mathbf{k} + \mathbf{p}_\theta)\tilde{H}(\mathbf{k})$; similarly, $\tilde{S}_a(\mathbf{k} + \mathbf{p}_\theta)\tilde{H}(\mathbf{k}) = m\tilde{S}_o(\mathbf{k} + \mathbf{p}_\theta)\tilde{H}(\mathbf{k})$ and has no contribution from $\tilde{S}_o(\mathbf{k} - \mathbf{p}_\theta)\tilde{H}(\mathbf{k})$. This ensures that cross-correlation between $\tilde{S}_a(\mathbf{k} - \mathbf{p}_\theta)\tilde{H}(\mathbf{k})$ and $\tilde{S}_a(\mathbf{k} + \mathbf{p}_\theta)\tilde{H}(\mathbf{k})$ is minimum when $\psi_2 = \phi'_2$ and $\psi_3 = \phi'_3$. This fact is used to determine the unknown phases ϕ'_2 and ϕ'_3 [33].

Specifically, beginning with arbitrary initial guesses for unknown phases ϕ'_2 and ϕ'_3 , say ψ_2 and ψ_3 , respectively, $\tilde{S}_a(\mathbf{k} - \mathbf{p}_\theta)\tilde{H}(\mathbf{k})$ and $\tilde{S}_a(\mathbf{k} + \mathbf{p}_\theta)\tilde{H}(\mathbf{k})$ are computed using Eq. (36). Following this, we compute the cross-correlation

$$\mathcal{C}_4 = \sum_{\mathbf{k}} w(\mathbf{k}) \left(\tilde{S}_a(\mathbf{k} - \mathbf{p}_\theta)\tilde{H}(\mathbf{k}) \right) \left(\tilde{S}_a(\mathbf{k} + \mathbf{p}_\theta)\tilde{H}(\mathbf{k}) \right)^* \quad (38)$$

where $w(\mathbf{k})$ is a weighing function to minimize the effect of noise in $\tilde{S}_a(\mathbf{k} - \mathbf{p}_\theta)\tilde{H}(\mathbf{k})$ and $\tilde{S}_a(\mathbf{k} + \mathbf{p}_\theta)\tilde{H}(\mathbf{k})$ on the

computed value of \mathcal{C}_4 . Subsequently, the values of ψ_2 and ψ_3 are iteratively optimized to produce a minima for $|\mathcal{C}_4|$. Values of ψ_2 and ψ_3 for the optimum condition are taken to be the estimates of unknown phases ϕ'_2 and ϕ'_3 , respectively. For Gaussian noise, optimal weighing function is shown to be $w(\mathbf{k}) = \tilde{H}(\mathbf{k})\tilde{H}^*(\mathbf{k})$ [33].

C. Determination of Illumination Spatial Frequency \mathbf{p}_θ

An estimate of illumination spatial frequency \mathbf{p}_θ is obtained by iteratively optimizing \mathbf{p}_e to obtain a maxima for the normalized cross-power spectrum [47]

$$\mathcal{C}_5 = \left| \frac{\sum_{\mathbf{k}} \tilde{S}_{\text{central}}(\mathbf{k}) \tilde{S}_{\text{side}}^*(\mathbf{k} + \mathbf{p}_e)}{\sum_{\mathbf{k}} \tilde{S}_{\text{side}}(\mathbf{k} + \mathbf{p}_e) \tilde{S}_{\text{side}}^*(\mathbf{k} + \mathbf{p}_e)} \right|. \quad (39)$$

The noisy estimates of $\tilde{S}_o(\mathbf{k})\tilde{H}(\mathbf{k})$ and $\tilde{S}_o(\mathbf{k} - \mathbf{p}_\theta)\tilde{H}(\mathbf{k})$ obtained in step 4 of Algorithm 2 are used to define the following intermediate terms which are required for evaluation of \mathcal{C}_5 .

$$\tilde{S}_{\text{central}}(\mathbf{k}) = [\tilde{S}(\mathbf{k})\tilde{H}(\mathbf{k})] \tilde{H}^*(\mathbf{k})$$

$$\tilde{S}_{\text{side}}(\mathbf{k}) = [\tilde{S}_o(\mathbf{k} - \mathbf{p}_\theta)\tilde{H}(\mathbf{k})] \tilde{H}^*(\mathbf{k})$$

$$\tilde{S}_{\text{side}}(\mathbf{k} + \mathbf{p}_e) = \mathcal{F} \left[\left\{ \mathcal{F}^{-1} \tilde{S}_{\text{side}}(\mathbf{k}) \right\} \times e^{-i2\pi(\mathbf{p}_e \cdot \mathbf{r})} \right].$$

The fact that the overlapping frequency contents of $\tilde{S}(\mathbf{k})\tilde{H}(\mathbf{k})$ and $\tilde{S}_o(\mathbf{k} - \mathbf{p}_\theta)\tilde{H}(\mathbf{k})$, shifted to its correct location, are correlated, ensures that \mathcal{C}_5 achieves its maxima when $\mathbf{p}_e = \mathbf{p}_\theta$.

D. Remarks on Algorithm 2

1) Algorithm 1 estimates illumination spatial frequency first and then estimates illumination phase. In Algorithm 2, this order is reversed.

2) Unlike Algorithm 1, Algorithm 2 never estimates true illumination phases ϕ_1 , ϕ_2 and ϕ_3 . Algorithm 2 estimates relative phases $\phi'_2 (= \phi_2 - \phi_1)$ and $\phi'_3 (= \phi_3 - \phi_1)$ in step 3. The information of phase ϕ_1 is absorbed within estimates of $\tilde{S}_o(\mathbf{k} - \mathbf{p}_\theta)$ and $\tilde{S}_o(\mathbf{k} + \mathbf{p}_\theta)$ computed in step 4. During subsequent steps of Algorithm 2, the information of phase ϕ_1 propagates to $\tilde{S}_s(\mathbf{k} - \mathbf{p}_\theta)$ and $\tilde{S}_s(\mathbf{k} + \mathbf{p}_\theta)$ computed in step 11. Eventually, the “phase matching” effected in step 12 relieves $\tilde{S}_s(\mathbf{k} - \mathbf{p}_\theta)$ and $\tilde{S}_s(\mathbf{k} + \mathbf{p}_\theta)$ of the information of phase ϕ_1 contained within them. Thus, unlike the “phase matching” step of Algorithm 1, which serves to correct the minor imprecisions in the estimation of absolute illumination phases ϕ_1 , ϕ_2 and ϕ_3 , the “phase matching” step of Algorithm 2 compensates for the fact that all prior computations were carried out using the estimates of relative illumination phases ϕ'_2 and ϕ'_3 .

3) Algorithm 2 may also be used to carry out SIM image reconstruction when illumination spatial frequency lies within the OTF support, as for the cases depicted in Figs. 4 and 6. The reconstructed SIM images, for both simulated and experimental cases described in Section VI, obtained using Algorithm 2 were found to be visually similar to that depicted in Figs. 4 and 6.

Algorithm 2: TIRF-SIM-RA

```

1 function TIRF-SIM ;
  Input : System OTF  $\tilde{H}(\mathbf{k})$  and nine raw SIM images  $D_{\theta,\phi}(\mathbf{r})$ , corresponding to  $\theta = \theta_1, \theta_2, \theta_3$  and  $\phi = \phi_1, \phi_2, \phi_3$ 
  Output: Reconstructed SIM image  $D_{SIM}(\mathbf{r})$ 
2 for  $\{D_{\theta,\phi}(\mathbf{r}) | \theta = \theta_1, \theta_2, \theta_3\}$  do
3   Estimate phases  $\phi'_2$  and  $\phi'_3$  (section VIII-B);
4   Obtain noisy estimates of  $\tilde{S}(\mathbf{k})\tilde{H}(\mathbf{k})$ ,  $\tilde{S}_o(\mathbf{k} - \mathbf{p}_\theta)\tilde{H}(\mathbf{k})$  and  $\tilde{S}_o(\mathbf{k} + \mathbf{p}_\theta)\tilde{H}(\mathbf{k})$  using Eq. (34) (do this by setting  $m = 1$  in matrix  $\mathbf{M}_o$  [Eq. (33)]; Adjustment for  $m \neq 1$  is effected later in steps 9 and 10 below) ;
5   Estimate illumination spatial frequency  $\mathbf{p}_\theta$  (section VIII-C);
6 end
7 Average the three noisy estimates of  $\tilde{S}(\mathbf{k})\tilde{H}(\mathbf{k})$  (one for each  $\theta = \theta_1, \theta_2, \theta_3$ ) and use it to estimate parameters  $\mathcal{A}$  and  $\alpha$  characterizing object power spectrum (section IV-C) ;
8 for  $\theta = \theta_1, \theta_2, \theta_3$  do
9   Determine modulation factor  $m$  (following the line of reasoning provided in section IV-D);
10  Use Wiener Filter to obtain noise-filtered and ungraded estimates  $\tilde{S}_u(\mathbf{k})$ ,  $\tilde{S}_u(\mathbf{k} - \mathbf{p}_\theta)$  and  $\tilde{S}_u(\mathbf{k} + \mathbf{p}_\theta)$  of noisy  $\tilde{S}(\mathbf{k})\tilde{H}(\mathbf{k})$ ,  $\tilde{S}_o(\mathbf{k} - \mathbf{p}_\theta)\tilde{H}(\mathbf{k})$  and  $\tilde{S}_o(\mathbf{k} + \mathbf{p}_\theta)\tilde{H}(\mathbf{k})$ , respectively (section IV-E; Note: This requires replacing  $\tilde{S}(\mathbf{k} - \mathbf{p}_\theta)\tilde{H}(\mathbf{k})$  and  $\tilde{S}(\mathbf{k} + \mathbf{p}_\theta)\tilde{H}(\mathbf{k})$  in Eqs. (12) and (13) with  $\tilde{S}_o(\mathbf{k} - \mathbf{p}_\theta)\tilde{H}(\mathbf{k})$  and  $\tilde{S}_o(\mathbf{k} + \mathbf{p}_\theta)\tilde{H}(\mathbf{k})$ , respectively. );
11  Shift  $\tilde{S}_u(\mathbf{k} - \mathbf{p}_\theta)$  and  $\tilde{S}_u(\mathbf{k} + \mathbf{p}_\theta)$  components to their respective true positions in frequency domain (section IV-F).
    Let  $\tilde{S}_s(\mathbf{k} - \mathbf{p}_\theta)$  and  $\tilde{S}_s(\mathbf{k} + \mathbf{p}_\theta)$ , respectively, denote components  $\tilde{S}_u(\mathbf{k} - \mathbf{p}_\theta)$  and  $\tilde{S}_u(\mathbf{k} + \mathbf{p}_\theta)$  shifted to their true positions;
12  ‘Phase match’ the shifted components  $\tilde{S}_s(\mathbf{k} - \mathbf{p}_\theta)$  and  $\tilde{S}_s(\mathbf{k} + \mathbf{p}_\theta)$  with respect to the unshifted component  $\tilde{S}_u(\mathbf{k})$  (section IV-G) ;
13 end
14 Merge all nine frequency frequency components (three components  $\tilde{S}_u(\mathbf{k})$ ,  $\tilde{S}_s(\mathbf{k} - \mathbf{p}_\theta)$  and  $\tilde{S}_s(\mathbf{k} + \mathbf{p}_\theta)$  for each of the three  $\theta$ s) into one  $\tilde{D}_{SIM}(\mathbf{k})$  using generalized Wiener-Filter (section IV-H) ;
15 Compute inverse FT of  $\tilde{D}_{SIM}(\mathbf{k})$  to obtain reconstructed SIM image  $D_{SIM}(\mathbf{r})$  ;
16 return  $D_{SIM}(\mathbf{r})$  ;

```

IX. CONCLUSION

In the family of super-resolution microscopy, SIM plays an important role because it brings insight from the view point of frequency domain, whereas other techniques primarily do so from the spatial domain. It requires the interference between the illumination spatial frequency and the sample frequency, so that the differential frequency falling within the OTF support of the microscopic objective can be detected. Such modulation with illumination pattern is done at several different angles and phases. Consequently, a post-processing to bring the relevant frequency components back to their original coordinates in frequency domain, is necessary. In this study, we collect all the details—such as the determination of the illumination spatial frequency, phase shifts, objective power spectrum, modulation factor, phase shift error, translocation and merging of various frequency components—into one coherent piece to build a SIM-RA. Following this, we demonstrate efficacy of SIM-RA for simulated SIM images. Specifically, we studied the resolution enhancement that may be achieved through direct deconvolution (Wiener filtering) and SIM reconstruction by computing effective PSFs. Previously, the $2\times$ resolution enhancement of SIM has always been assessed in frequency domain, but never been illustrated in spatial domain with PSF width computation. Here we show that, deconvolution such as Wiener filtering can provide $\approx 1.4\times$ resolution enhancement, whereas SIM provides $\approx 2\times$ resolution enhancement in term of reduction in PSF width. Further, we demonstrate the efficacy of SIM-RA for

experimental SIM data, by high-resolution image reconstruction of the microtubules in COS7 cell.

The SIM-RA as described in the manuscript, is coded into a series of MATLAB-based script and function files. This complete set of files, collectively called as OpenSIM, is freely made available as a companion to this manuscript. This is to enable the users to better understand the algorithm, and to manipulate the parameters interactively, so that the errors/artifacts of SIM reconstruction can be minimized. It is hoped that readers from both instrumentation background and biological background may find this paper resourceful.

In this study, we have restricted our discussion on 2-D SIM. Based on the same principle, 3-D SIM can also be done in a similar manner, which is an ongoing project of the authors.

APPENDIX A WIENER FILTERING MULTIPLE BUT NON IDENTICAL IMAGES OF SAME OBJECT

Let $G_i(\mathbf{r})$ be a set of n images capturing different views $S_i(\mathbf{r})$ of same object $S(\mathbf{r})$, such that

$$G_i(\mathbf{r}) = S_i(\mathbf{r}) \otimes H_i(\mathbf{r}) + N_i(\mathbf{r}) \quad \{i = 1, 2, \dots, n\} \quad (40)$$

where $H_i(\mathbf{r})$ is system PSF and $N_i(\mathbf{r})$ is additive noise in each image. In fourier domain, Eq. (40) is given by

$$\tilde{G}_i(\mathbf{k}) = \tilde{S}_i(\mathbf{k})\tilde{H}_i(\mathbf{k}) + \tilde{N}_i(\mathbf{k}) \quad \{i = 1, 2, \dots, n\}. \quad (41)$$

In such situation, an estimate $S_a(\mathbf{r})$ of ungraded object $S(\mathbf{r})$ is provided by generalized Wiener Filter [48]

$$\tilde{S}_a(\mathbf{k}) = \sum_{i=1}^n \left[\frac{\Phi_i(\mathbf{k})|\tilde{H}_i(\mathbf{k})|^2/\Psi_i}{1 + \sum_{i=1}^n \Phi_i(\mathbf{k})|\tilde{H}_i(\mathbf{k})|^2/\Psi_i} \right] \frac{\tilde{G}_i(\mathbf{k})}{\tilde{H}_i(\mathbf{k})} \quad (42)$$

where

$$|\tilde{H}_i(\mathbf{k})|^2 = \tilde{H}_i(\mathbf{k})\tilde{H}_i^*(\mathbf{k}) = \text{power spectrum of } i\text{th OTF}$$

$$\Psi_i = \text{average noise power in } i\text{th image}$$

$$\Phi_i(\mathbf{k}) = |\tilde{S}_i(\mathbf{k})|^2 = \text{mean power spectrum of } i\text{th ungraded image.}$$

A. Approximation to Generalized Wiener Filter

Conventional Wiener Filter estimate of $\tilde{S}_i(\mathbf{k})$ is given by

$$\tilde{S}_{o,i}(\mathbf{k}) = \left[\frac{|\tilde{H}_i(\mathbf{k})|^2}{|\tilde{H}_i(\mathbf{k})|^2 + \Psi_i/\Phi_i(\mathbf{k})} \right] \frac{\tilde{G}_i(\mathbf{k})}{\tilde{H}_i(\mathbf{k})}. \quad (43)$$

Approximating $\tilde{G}_i(\mathbf{k})/\tilde{H}_i(\mathbf{k}) \approx \tilde{S}_{o,i}(\mathbf{k})$ (note: this approximation becomes equality when noise power $\Psi_i = 0$), Eq. (42) may be modified as

$$\tilde{S}_a(\mathbf{k}) = \sum_{i=1}^n \left[\frac{\Phi_i(\mathbf{k})|\tilde{H}_i(\mathbf{k})|^2/\Psi_i}{w + \sum_{i=1}^n \Phi_i(\mathbf{k})|\tilde{H}_i(\mathbf{k})|^2/\Psi_i} \right] \tilde{S}_{o,i}(\mathbf{k}). \quad (44)$$

Note that the additive constant 1 in denominator of Eq. (42) is replaced by a constant parameter w whose value needs to be empirically set. Since, $S_{o,i}(\mathbf{k})$ is already noise-filtered, Eq. (43), suitable value of parameter w may be empirically searched for in the range $\{0 < w \leq 1\}$.

APPENDIX B EFFECTIVE PSF DETERMINATION

It is possible to express the convolution operation between “object” and PSF resulting in “image” formation in the form of a matrix multiplication equation, see Fig. 7.

Consequently, when both “object” and “image” are known, it is possible to estimate the unknown PSF. Begin with a wise estimate of the size of PSF, say $p \times p$. Then using the “object” and “image,” construct a matrix O and a vector I , as illustrated in Fig. 7, both with number of rows $r > p^2$. Note that, first, vector I is formed by randomly selecting $r > p^2$ image pixels (all these pixels must be more than half PSF width away from image edge) and arranging them into a column vector. Corresponding to each image pixel that is selected for constructing I , its corresponding sub-matrix in object is located; elements of this sub-matrix are rearranged to form row of matrix O . Since, $O \times P = I$, least square solution for PSF vector P is given by $P = (O^T O)^{-1} O^T I$. Subsequently, elements of vector P may be rearranged to obtain two-dimension PSF of size $p \times p$.

For determination of both $\text{PSF}_{\text{deconvWF}}$ and PSF_{SIM} (see Section VI-A2), PSF size was assumed to be 40×40 pixels. While solving for PSFs, matrix O and vector I were constructed with number of rows $r = 7 \times 40 \times 40$. By constructing different pairs O and I , PSF vector P was solved for, 100 times; mean of all these estimated P s was then used to reconstruct the PSF under determination, eventually.

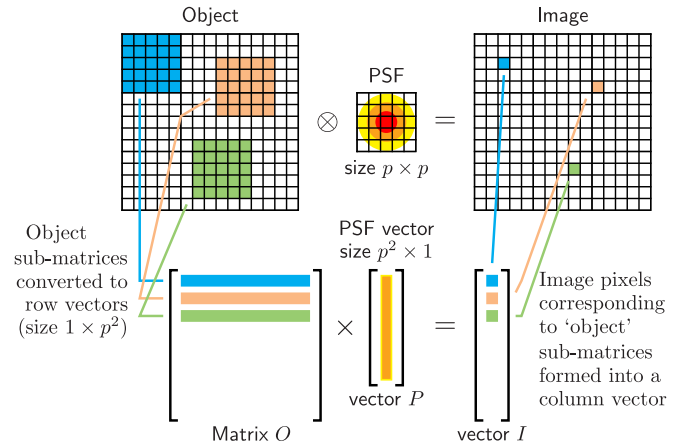


Fig. 7. Top Panel: Each “image” pixel which is more than half PSF width away from edge is obtained as a result of weighted-average of a sub-matrix of “object” with PSF. Bottom panel: By appropriately rearranging the elements of object’s sub-matrix into a row vector and that of PSF’s into a column vector (P), this weighted-average operation may be expressed as product of these row and column vectors. Consequently, a matrix equation: $O \times P = I$ may be formed. This equation may be used to estimate PSF, in case when it is unknown but “object” and “image” are known.

ACKNOWLEDGMENT

The authors would like to thank Prof. S. Tang and Prof. K. Satish for helpful discussions.

REFERENCES

- [1] P. S. Weiss, “Nobel prizes for super-resolution imaging,” *ACS Nano*, vol. 8, no. 10, pp. 9689–9690, 2014.
- [2] S. Hell, “Far-field optical nanoscopy,” in *Single Molecule Spectroscopy in Chemistry, Physics and Biology*, ser. Springer Series in Chemical Physics, vol. 96, A. Gräslund, R. Rigler, and J. Widengren, Eds. New York, NY, USA: Springer, 2010, pp. 365–398.
- [3] S. W. Hell and J. Wichmann, “Breaking the diffraction resolution limit by stimulated emission: Stimulated-emission-depletion fluorescence microscopy,” *Opt. Lett.*, vol. 19, no. 11, pp. 780–782, 1994.
- [4] J. Liu *et al.*, “Achieving $\lambda/10$ resolution CW sted nanoscopy with a Ti:Sapphire oscillator,” *Plos One*, vol. 7, no. 6, p. e40003, 2012.
- [5] X. Yang *et al.*, “Sub-diffraction imaging of nitrogen-vacancy centers in diamond by stimulated emission depletion and structured illumination,” *RSC Adv.*, vol. 4, no. 22, pp. 11305–11310, 2014.
- [6] X. Chen *et al.*, “Subdiffraction optical manipulation of the charge state of nitrogen vacancy center in diamond,” *Light: Sci. Appl.*, vol. 4, no. 1, p. e230, 2015.
- [7] K. Fujita, M. Kobayashi, S. Kawano, M. Yamanaka, and S. Kawata, “High-resolution confocal microscopy by saturated excitation of fluorescence,” *Phys. Rev. Lett.*, vol. 99, no. 22, p. 228105, 2007.
- [8] M. G. Gustafsson, “Surpassing the lateral resolution limit by a factor of two using structured illumination microscopy,” *J. Microscopy*, vol. 198, no. 2, pp. 82–87, 2000.
- [9] E. Betzig *et al.*, “Imaging intracellular fluorescent proteins at nanometer resolution,” *Science*, vol. 313, no. 5793, pp. 1642–1645, 2006.
- [10] S. T. Hess, T. P. Girirajan, and M. D. Mason, “Ultra-high resolution imaging by fluorescence photoactivation localization microscopy,” *Biophys. J.*, vol. 91, no. 11, pp. 4258–4272, 2006.
- [11] M. J. Rust, M. Bates, and X. Zhuang, “Sub-diffraction-limit imaging by stochastic optical reconstruction microscopy (STORM),” *Nature Methods*, vol. 3, no. 10, pp. 793–796, 2006.
- [12] T. Dertinger, R. Colyer, G. Iyer, S. Weiss, and J. Enderlein, “Fast, background-free, 3d super-resolution optical fluctuation imaging (SOFI),” *Proc. Nat. Acad. Sci. USA*, vol. 106, no. 52, pp. 22287–22292, 2009.
- [13] T. Dertinger, R. Colyer, R. Vogel, M. Heilemann, M. Sauer, J. Enderlein, and S. Weiss, “Superresolution optical fluctuation imaging (SOFI),” in *Proc. Nano-Biotechnol. Biomed. Diagnostic Res.*, 2012, pp. 17–21.

- [14] Z. Zeng *et al.*, "Fast super-resolution imaging with ultra-high labeling density achieved by joint tagging super-resolution optical fluctuation imaging," *Sci. Rep.*, vol. 5, 2015.
- [15] Y. Deng, M. Sun, P.-H. Lin, J. Ma, and J. W. Shaeitz, "Spatial covariance reconstructive (SCORE) super-resolution fluorescence microscopy," *PloS One*, vol. 9, no. 4, 2014.
- [16] A. N. Kapanidis and T. Strick, "Biology, one molecule at a time," *Trends Biochemical Sci.*, vol. 34, no. 5, pp. 234–243, 2009.
- [17] P. Kner, B. B. Chhun, E. R. Griffis, L. Winoto, and M. G. Gustafsson, "Super-resolution video microscopy of live cells by structured illumination," *Nature Methods*, vol. 6, no. 5, pp. 339–342, 2009.
- [18] D. Li *et al.*, "Extended-resolution structured illumination imaging of endocytic and cytoskeletal dynamics," *Science*, vol. 349, no. 6251, p. aab3500, 2015.
- [19] F. Wei and Z. Liu, "Plasmonic structured illumination microscopy," *Nano Lett.*, vol. 10, no. 7, pp. 2531–2536, 2010.
- [20] J. Mertz and J. Kim, "Scanning light-sheet microscopy in the whole mouse brain with HiLo background rejection," *J. Biomed. Opt.*, vol. 15, no. 1, pp. 016027–016027, 2010.
- [21] J. Mertz, "Optical sectioning microscopy with planar or structured illumination," *Nature Methods*, vol. 8, no. 10, pp. 811–819, 2011.
- [22] P. J. Keller *et al.*, "Fast, high-contrast imaging of animal development with scanned light sheet-based structured-illumination microscopy," *Nature Methods*, vol. 7, no. 8, pp. 637–642, 2010.
- [23] B.-C. Chen *et al.*, "Lattice light-sheet microscopy: Imaging molecules to embryos at high spatiotemporal resolution," *Science*, vol. 346, no. 6208, p. 1257998, 2014.
- [24] L. Gao, "QSIM: Quantitative structured illumination microscopy image processing in imagej," *Biomed. Eng. Online*, vol. 14, no. 1, p. 4, 2015.
- [25] M. G. Gustafsson, "Nonlinear structured-illumination microscopy: Wide-field fluorescence imaging with theoretically unlimited resolution," *Proc. Nat. Acad. Sci. USA*, vol. 102, no. 37, pp. 13081–13086, 2005.
- [26] E. H. Rego *et al.*, "Nonlinear structured-illumination microscopy with a photoswitchable protein reveals cellular structures at 50-nm resolution," *Proc. Nat. Acad. Sci. USA*, vol. 109, no. 3, pp. E135–E143, 2012.
- [27] O. Schulz *et al.*, "Resolution doubling in fluorescence microscopy with confocal spinning-disk image scanning microscopy," *Proc. Nat. Acad. Sci. USA*, vol. 110, no. 52, pp. 21000–21005, 2013.
- [28] C. B. Müller and J. Enderlein, "Image scanning microscopy," *Phys. Rev. Lett.*, vol. 104, no. 19, p. 198101, 2010.
- [29] E. Mudry *et al.*, "Structured illumination microscopy using unknown speckle patterns," *Nature Photon.*, vol. 6, no. 5, pp. 312–315, 2012.
- [30] R. Heintzmann and C. G. Cremer, "Laterally modulated excitation microscopy: Improvement of resolution by using a diffraction grating," *Proc. SPIE*, vol. 3568, pp. 185–196, 1999.
- [31] L. Schaefer, D. Schuster, and J. Schaffer, "Structured illumination microscopy: Artefact analysis and reduction utilizing a parameter optimization approach," *J. Microscopy*, vol. 216, no. 2, pp. 165–174, 2004.
- [32] S. A. Shroff, J. R. Fienup, and D. R. Williams, "Lateral superresolution using a posteriori phase shift estimation for a moving object: Experimental results," *J. Opt. Soc. Amer. A*, vol. 27, no. 8, pp. 1770–1782, 2010.
- [33] K. Wicker, O. Mandula, G. Best, R. Fiolka, and R. Heintzmann, "Phase optimisation for structured illumination microscopy," *Opt. Expr.*, vol. 21, no. 2, pp. 2032–2049, 2013.
- [34] K. Wicker, "Non-iterative determination of pattern phase in structured illumination microscopy using auto-correlations in fourier space," *Opt. Expr.*, vol. 21, no. 21, pp. 24692–24701, 2013.
- [35] L. Shao, "Image reconstruction for structured-illumination microscopy implemented in CUDA [Online]. Available: https://github.com/landobbie/CUDA_SIMRecon
- [36] P. Krížek, T. Lukeš, M. Ovesný, K. Fliegel, and G. M. Hagen, "Simtoolbox: A matlab toolbox for structured illumination fluorescence microscopy," *Bioinformatics*, vol. 32, no. 2, pp. 318–320, 2015.
- [37] G. Ball, J. Demmerle, R. Kaufmann, I. Davis, I. M. Dobbie, and L. Schermelleh, "Simcheck: A toolbox for successful super-resolution structured illumination microscopy," *Sci. Rep.*, vol. 5, 2015.
- [38] F. Orioux, E. Sepulveda, V. Loriette, B. Dubertret, and J.-C. Olivo-Marin, "Bayesian estimation for optimized structured illumination microscopy," *IEEE Trans. Image Process.*, vol. 21, no. 2, pp. 601–614, Feb. 2012.
- [39] S. Dong *et al.*, "Resolution doubling with a reduced number of image acquisitions," *Biomed. Opt. Exp.*, vol. 6, no. 8, pp. 2946–2952, 2015.
- [40] R. C. Gonzalez and R. E. Woods, *Digital Image Processing*. Englewood Cliffs, NJ, USA: Prentice-Hall, 2002.
- [41] J. R. Fienup *et al.*, "Comparison of reconstruction algorithms for images from sparse-aperture systems," in *Proc. Int. Symp. Opt. Sci. Technol.*, 2002, pp. 1–8.
- [42] J. D. Gaskill, *Linear Systems, Fourier Transforms, and Optics*, vol. 1. New York, NY, USA: Wiley, 1978.
- [43] University of Southern California, Signal and Image Processing Institute, The USC-SIPI image database [Online]. Available: <http://sipi.usc.edu/database/>
- [44] K. Wicker and R. Heintzmann, "Resolving a misconception about structured illumination," *Nature Photon.*, vol. 8, no. 5, pp. 342–344, 2014.
- [45] MATLAB & Simulink - MathWorks. Basic image enhancement and analysis techniques [Online]. Available: <http://cn.mathworks.com/help/images/image-enhancement-and-analysis.html>
- [46] M. G. Gustafsson *et al.*, "Three-dimensional resolution doubling in wide-field fluorescence microscopy by structured illumination," *Biophys. J.*, vol. 94, no. 12, pp. 4957–4970, 2008.
- [47] H. Foroosh, J. B. Zerubia, and M. Berthod, "Extension of phase correlation to subpixel registration," *IEEE Trans. Image Process.*, vol. 11, no. 3, pp. 188–200, Mar. 2002.
- [48] L. P. Yaroslavsky and H. J. Caulfield, "Deconvolution of multiple images of the same object," *Appl. Opt.*, vol. 33, no. 11, pp. 2157–2162, 1994.

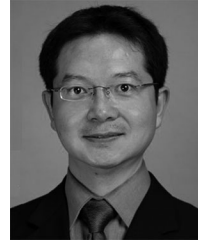


Amit Lal received the Ph.D. degree from the Indian Institute of Science, Bangalore, India. Following this, he was a Research Assistant for three years in the field of Respiratory Neuroscience at Hyogo College of Medicine, Nishinomiya, Japan. He is currently a Doctorate student in the Department of Biomedical Engineering, College of Engineering, Peking University, Beijing, China.



Chunyan Shan received the Ph.D. degree from the School of Life Sciences, Peking University, Beijing, China. Afterwards, she did her postdoctoral study in Core Facilities of Life Sciences, Peking University. Since 2015, she works in Core Facilities of Life Sciences, Peking University as an Engineer.

His current research interests include application of super-resolution microscopy in cell biology, for instance, live-cell super-resolution imaging, ultrastructure analysis using SIM, STED, and STORM.



Peng Xi received the Ph.D. degree from the Shanghai Institute of Optics and Fine Mechanics, Chinese Academy of Sciences, Shanghai, China. He then was a Postdoctoral Research Associate in three universities: Hong Kong University of Science and Technology, Purdue University, and Michigan State University. From 2008 to 2009, he was with the Department of Biomedical Engineering, Shanghai Jiao Tong University as an Associate Professor. He is currently working in the Department of Biomedical Engineering, College of Engineering, Peking University as an Associate Professor since 2009.

His current research interests include research and development of optical nanoscopy, as well as confocal and multiphoton microscopy. He has published more than 40 scientific papers in peer-reviewed journals such as *Nature Photonics*, *ACS Nano*, *Scientific Reports*, *Optics Letters*, *Optics Express*, etc., and received seven issued patents, including two US patents.

Dr. Peng Xi is on the editorial board of several SCI-indexed journals: *Scientific Reports*, *Micron*, *Microscopy Research and Techniques*, and *Chinese Optics Letters*. He has been invited to give several invited talks in international conferences hosted by IEEE, OSA, and SPIE.